The Meteoritical Society

Meteoritics & Planetary Science 46, Nr 9, 1227–1252 (2011)
doi: 10.1111/j.1945-5100.2011.01210.x

Thermal and impact histories of reheated group IVA, IVB, and ungrouped iron meteorites and their parent asteroids

J. YANG[1,2*], J. I. GOLDSTEIN[1], E. R. D. SCOTT[3], J. R. MICHAEL[4], P. G. KOTULA[4], T. PHAM[1], and T. J. McCOY[5]

[1]Department of Mechanical and Industrial Engineering, University of Massachusetts, Amherst, Massachusetts 01003, USA
[2]Carl Zeiss NTS, LLC, One Corporation Way, Peabody, Massachusetts 01960, USA
[3]Hawaii Institute of Geophysics and Planetology, University of Hawaii at Manoa, Honolulu, Hawaii 96822, USA
[4]Materials Characterization Department, Sandia National Laboratories, P.O. Box 5800, MS 0886, Albuquerque, New Mexico 87185, USA
[5]Department of Mineral Sciences, National Museum of Natural History, Smithsonian Institution, Washington, District of Columbia 20560, USA
[*]Corresponding author. E-mail: jiyang@ecs.umass.edu

(Received 20 December 2010; revision accepted 21 April 2011)

Abstract–The microstructures of six reheated iron meteoritesötwo IVA irons, Maria Elena (1935), Fuzzy Creek; one IVB iron, Ternera; and three ungrouped irons, Hammond, Babb's Mill (Blake's Iron), and Babb's Mill (Troost's Iron)öwere characterized using scanning and transmission electron microscopy, electron-probe microanalysis, and electron backscatter diffraction techniques to determine their thermal and shock history and that of their parent asteroids. Maria Elena and Hammond were heated below approximately 700–750 °C, so that kamacite was recrystallized and taenite was exsolved in kamacite and was spheroidized in plessite. Both meteorites retained a record of the original WidmanstÌtten pattern. The other four, which show no trace of their original microstructure, were heated above 600–700 °C and recrystallized to form 10–20 μm wide homogeneous taenite grains. On cooling, kamacite formed on taenite grain boundaries with their close-packed planes aligned. Formation of homogeneous 20 μm wide taenite grains with diverse orientations would have required as long as approximately 800 yr at 600 °C or approximately 1 h at 1300 °C. All six irons contain approximately 5–10 μm wide taenite grains with internal microprecipitates of kamacite and nanometer-scale M-shaped Ni profiles that reach approximately 40% Ni indicating cooling over 100–10,000 yr. Un-decomposed high-Ni martensite (α_2) in taeniteöthe first occurrence in ironsöappears to be a characteristic of strongly reheated irons. From our studies and published work, we identified four progressive stages of shock and reheating in IVA irons using these criteria: cloudy taenite, M-shaped Ni profiles in taenite, Neumann twin lamellae, martensite, shock-hatched kamacite, recrystallization, microprecipitates of taenite, and shock-melted troilite. Maria Elena and Fuzzy Creek represent stages 3 and 4, respectively. Although not all reheated irons contain evidence for shock, it was probably the main cause of reheating. Cooling over years rather than hours precludes shock during the impacts that exposed the irons to cosmic rays. If the reheated irons that we studied are representative, the IVA irons may have been shocked soon after they cooled below 200 °C at 4.5 Gyr in an impact that created a rubblepile asteroid with fragments from diverse depths. The primary cooling rates of the IVA irons and the proposed early history are remarkably consistent with the Pb-Pb ages of troilite inclusions in two IVA irons including the oldest known differentiated meteorite (Blichert-Toft et al. 2010).

∅ The Meteoritical Society, 2011.

INTRODUCTION

Many meteorites have been shocked by impacts on their parent bodies causing deformation, heating, and, in some cases, phase transformations (StÖffler et al. 1988, 1991; Leroux 2001; Sharp and DeCarli 2006). Observations of these shocked meteorites combined with results of shock experiments, theoretical studies, and radiometric dating provide important constraints on the impact histories of the meteorites and their parent bodies. Detailed studies of shocked meteorites also allow us to identify samples that have been least affected by impacts (e.g., those with taenite grains that faithfully preserve their original Ni profiles), and supply information about the early igneous and thermal history of the meteorites and their parent bodies (Goldstein et al. 2009).

In most iron meteorites, the WidmanstÀtten patterns of oriented kamacite plates in large taenite crystals have not been significantly modified by shock or reheating (Buchwald 1975). Kamacite may show Neumann bands, which are mechanical twins caused by deformation or shocks of up to approximately 1 GPa. Higher shock pressures above 13 GPa cause kamacite to transform to a hexagonally close-packed structure (ε phase), which reverts to distorted kamacite on pressure release. With increasing shock level, however, higher postshock temperatures cause significant changes in the microstructure and microchemistry of iron meteorites (Axon 1962; Miyake and Goldstein 1974; Buchwald 1975; Scott 1982; Goldstein et al. 2009). Irons can lose their cloudy zone microstructure and show localized recrystallization of WidmanstÀtten kamacite, formation of taenite grain boundaries, and submicrometer-scale Ni diffusion in taenite at kamacite–taenite boundaries. These features were observed using electron microscopy techniques in five IVA irons, Altonah, Gibeon, Jamestown, Obernkirchen, and Seneca Township (Goldstein et al. 2009) and two IVB irons, Skookum and Santa Clara (Yang et al. 2010). Diffusion calculations suggest that the cloudy taenite intergrowth, which has dimensions of approximately 20 nm in these irons, could have been removed by heating to 1000 °C for seconds, for example, or 500 °C for years (Goldstein et al. 2009).

Heavily shocked kamacite recrystallizes when shock pressures exceed approximately 70 GPa and postshock temperatures exceed approximately 500 °C (Heymann et al. 1966; StÖffler et al. 1988), which is near the recrystallization temperature of deformed pure iron of approximately 400–450 °C (Mitchell 2003). Recrystallization produces strain-free kamacite and taenite grains whose size is a function of the combination of time and temperature, and is more rapid than bulk diffusion. Usually reheating is insufficient to erase the WidmanstÀtten pattern. However, in a few rare irons such as Juromenha (IIIAB), Ternera (IVB), and Washington County (ungrouped), severe reheating has completely erased the original WidmanstÀtten pattern, presumably as a result of intense shock (Buchwald 1975). Even rarer are iron meteorites that were melted and rapidly cooled, and so they solidified with a dendritic microstructure (Axon 1962; Miyake and Goldstein 1974; Schrader et al. 2010).

Although most shocked and reheated iron meteorites are well characterized optically (Buchwald 1975), it is not clear that shock was the only process that caused reheating, and there is no classification scheme for shocked iron meteorites, as there is for silicate-rich meteorites (StÖffler et al. 1991). Full understanding of the peak temperatures and subsequent cooling rates requires detailed studies of the chemical compositions of the micrometer and submicrometer-sized phases and their structures and crystallographic orientations. These studies can be performed using optical and scanning electron microscopy (SEM) to examine the microstructure at increasing higher magnifications, electron backscattered diffraction (EBSD), to determine the structure and orientation of the phases that develop at peak temperatures and during cooling, electron-probe microanalysis (EPMA) to determine the bulk, kamacite, and taenite composition; and scanning transmission electron microscopy (STEM) to obtain chemical information at the nm scale to examine chemical reactions and diffusion associated with phase transformations that take place during reheating and subsequent cooling. The purpose of this study is: (1) to observe and characterize the microstructure of several reheated iron meteorites using electron microscopy techniques, (2) to determine the time–temperature history necessary to form these microstructures, and (3) to integrate this information with our existing knowledge of the shock and thermal history of iron meteorites to elucidate their impact history and origin.

METHODS

As we have recently studied the igneous and thermal history of groups IVA and IVB (Yang et al. 2007, 2008, 2010; Goldstein et al. 2009), we selected two reheated IVA irons, Fuzzy Creek and Maria Elena (1935), and one reheated IVB iron, Ternera, for study. In addition, we chose three ungrouped irons, Babb's Mill (Blake's Iron), Babb's Mill (Troost's Iron), and Hammond, to obtain a wider range of alteration microstructures. Table 1 summarizes the microstructure, meteorite classification, and source of the six meteorites we studied.

Table 1. Reheated iron meteorites and their sample source, group, and structure.

Meteorite	Source	Group	WidmanstÄtten	Microstructure
Maria Elena	USNM 1221b	IVA	Relic	Partly recryst. K + T
Hammond	USNM 471b	Ungrouped	Relic	Largely recryst. K + T + Ph
Ternera	USNM 1231	IVB	Absent	Fully recryst. K + T + Ph
Fuzzy Creek	USNM 6874	IVA	Absent	Fully recryst. K + T + Ph
Babb's Mill (Blake's Iron)	NHMV	Ungrouped	Absent	Fully recryst. K + T
Babb's Mill (Troost's Iron)	ASU 2905	Ungrouped Ć (So. Byron trio)	Absent	Fully recryst. K + T + Ph

Note: NHMV = Natural History Museum Vienna; USNM = US National Museum of Natural History; ASU = Arizona State University; recryst. = recrystallized; K = kamacite; T = taenite; Ph = phosphide $(Fe\text{-}Ni)_3P$.

The meteorite samples were prepared for optical microscopy and SEM of the meteorite microstructures using standard metallographic procedures: mounting, grinding, polishing, and etching with 2% nital. SEM studies were accomplished using a ZEISS EVO 50 at UMass, and a ZEISS Supra 55VP SEM at Sandia National Laboratories. A CAMECA SX-50 EPMA was used to determine the bulk composition of some of the meteorites and to measure the average composition of kamacite, phosphide, and taenite–kamacite intergrowths in the six reheated meteorites. The samples for EPMA were prepared using standard metallographic procedures, but were not etched. A beam voltage of 15 kV and a beam current of 40 nA were used. Pure metals that served as standards for Fe, Ni, Co, and $(Fe\text{-}Ni)_3P$ in the Grant meteorite was used as the P standard. Counting times for peak and background measurements were 30 s for Fe and Ni, 40 s for Co, and 60 s for P. The bulk Fe, Ni, Co, and P compositions of the samples were measured by averaging several line and ⊇ or area scans. For bulk composition measurements, the total area analyzed for each meteorite was determined by the amount, size, and distribution of phosphides, and was 15,000 μm^2 or larger. (The Co data, which were only used to help identify phases and samples, were not corrected for the small overlap between FeKβ and CoKα X-ray lines.)

Electron backscattered diffraction studies were performed using a ZEISS Supra 55VP SEM at Sandia National Laboratories, outfitted with an EBSD unit from Oxford Instruments with Channel 5 software (see Goldstein and Michael 2006). This technique allows body-centered cubic (bcc) and face centered cubic (fcc) Fe-Ni to be identified from their electron diffraction patterns, and the orientation of the bcc and fcc phases with respect to the sample placement (x, y, and z directions) in the SEM. In slow-cooled irons, the fcc phase is Ni-rich taenite (or ordered FeNi, tetrataenite which cannot be distinguished from taenite using EBSD), and the bcc is kamacite with < 7% Ni. However, impact-heated irons may also contain metastable bcc Fe-Ni with Ni contents of 10–28 wt%, viz., martensite formed directly from taenite by a shear transformation.

Meteorite samples were prepared for EBSD using standard metallographic polishing procedures followed by a two-step vibratory polishing procedure. The first vibratory polishing was performed using 0.1 μm Al_2O_3 for 4 h followed by a second vibratory polishing step using 0.04 μm SiO_2 for 2–4 h. Both vibratory polishing steps were carried out on napped cloth. This procedure removed surface deformation caused by standard metallographic polishing. Diffraction patterns were obtained using a beam voltage of 20 kV, a beam current of 1–2 nA, and a spot size diameter of < 2 nm. Orientation information was collected pixel-by-pixel with a pixel spacing of 0.02–0.5 μm. Orientation maps or inverse pole figure maps of the scanned specimen surface were developed using a color scheme to represent the orientation of the bcc and fcc phases with respect to the major poles (111, 100, 110) of the stereographic triangle. Thus, pixels with the same orientation have the same color. Sample regions shown in black could not be indexed as fcc or bcc Fe-Ni. They represent other phases such as schreibersite ($(Fe,Ni)_3P$) or troilite (FeS) or regions that could not be indexed because of surface roughness. Rogue or misindexed pixels are removed and then filled using a routine (eight nearest neighbor hole filling) that compares the surrounding pixels and fills in the missing ones. The orientation maps were used to determine local crystallographic orientations, which provide critical information necessary to understand how the various phases formed during reheating and subsequent cooling. Band contrast images, which resemble SEM backscattered electron images, were also used to show the quality of the EBSD pattern. Combined band contrast and orientation maps allow the distribution of bcc, fcc, and other phases to be readily compared.

Scanning transmission-analytical electron microscopy (STEM-AEM) was employed to characterize the chemical composition of taenite and kamacite at the nanometer scale. X-ray area scans for Fe and Ni were taken in micrometer and submicrometer-sized regions of the thin foil. High angle annular dark field STEM images, which show almost entirely compositional

Table 2. Bulk Ni and P concentrations determined using EPMA and literature values for reheated irons.

Meteorite	Ni (σ, wt%)	P (σ, wt%)
Maria Elena[a]	7.72	0.02
Hammond[b]	8.27	0.37
Ternera	17.2 0.39	0.20 0.04
Fuzzy Creek[c]	12.4	0.18
Babb's Mill Ć (Blake's Iron)	10.75 0.59	0.02 0.002
Babb's Mill Ć (Troost's Iron)	17.1 0.38	0.13 0.025

Note: Source of data for italicized irons: [a]Buchwald (1975); [b]Lewis and Moore (1971); [c]McCoy et al. (2011).

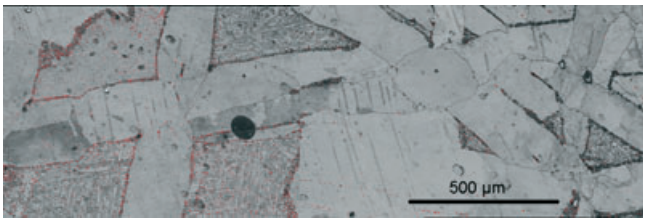

Fig. 1. EBSD band contrast map of Maria Elena with fcc phases in red showing the WidmanstÌtten pattern of oriented kamacite plates. At this magnification, the meteorite scarcely appears to have been reheated as only minor recrystallization of kamacite is visible.

(atomic number) contrast compared with normal TEM images, were used to locate regions of interest for the X-ray scanning images. The chemical information was extracted from the X-ray area scans, and was used to study the kinetics of the various phase transformations, particularly those that took place during cooling after the reheating event.

The iron meteorite samples were thinned for STEM analysis using a dual beam FEI DB-235 focused ion beam (FIB)⊇SEM instrument at Sandia National Laboratories. The STEM samples had a thickness of 50–100 nm and were approximately 10 µm long and 5 µm in width. Thin sections of selected regions were analyzed using a FEI Tecnai F30ST field emission TEM–AEM operated at 300 kV and housed at Sandia National Laboratories. Quantitative Ni gradients in taenite 0.5–2 µm in length were measured in a direction normal to kamacite–taenite interfaces using the stored EDS X-ray scan data. The X-ray data in each pixel were converted to composition using the Cliff–Lorimer method (Cliff and Lorimer 1975) with X-ray spatial resolution of 2–4 nm. A $k_{\text{Ni-Fe}}$ factor in the Cliff–Lorimer method of 1.10 was measured at 300 keV using a 25 wt% Ni-Fe standard.

RESULTS

Table 1 lists the microstructure, classification, and source of the six reheated iron meteorites and Table 2 lists the bulk Ni and P contents of these meteorites. The following subsections give the results of our observations and characterization of the microstructure of each reheated meteorite.

Maria Elena (IVA)

To the naked eye, Maria Elena has a normal WidmanstÌtten pattern with a fine octahedral structure like any other IVA iron with 7.7% Ni (Fig. 1) (Buchwald 1975). Partly obliterated sets of parallel Neumann twin lamellae are present in some kamacite regions. However, several anomalous features are visible in the WidmanstÌtten kamacite plates and in the interstitial regions between them that were once normal plessite fields and narrow taenite lamellae. Kamacite plates are partially recrystallized in some regions and show misoriented subgrains with sizes of 10–100 µm. The kamacite also contains ubiquitous micrometer-wide elongated particles of taenite that have exsolved on grain boundaries, Neumann bands, and within kamacite grains. These taenite particles are visible in Fig. 2a, which is an EPMA backscattered electron image showing a band of taenite grains about 25 µm wide between two kamacite plates, and in the EBSD map in Fig. 2b, which shows partly recrystallized kamacite plates next to two former plessite fields. In Fig. 2a, the taenite grains, which are mostly 2–5 µm in size, are partially spheroidized, forming somewhat rounded grains. No phosphide was observed consistent with the low P content (0.02 wt%).

The orientation of the taenite grains in Maria Elena can be inferred from the EBSD orientation maps in Fig. 2c and in Fig. 2d, which show a band of taenite grains at higher magnification. Taenite grains within the plessite fields in Fig. 2c appear to have retained the orientation of the original taenite crystal, as Goldstein and Michael (2006) observed in normal slow-cooled irons, but taenite grains at the border of the plessite field and in Figs. 2d and 2e show diverse orientations. Almost all taenite grains in the kamacite plates and the band of spheroidized taenite grains have a Kurdjumov–Sachs (K–S) or Nishiyama–Wassermann (N–W) {110}bcc⊇⊇{111}fcc orientation relationship with adjacent kamacite (Fig. 2e). (The two orientation relationships, which are defined in Table 3, are too similar to be distinguished using the EBSD technique.) Figure 2e also shows that many of the 2–5 µm wide spheroidized taenite grains themselves contain micrometer-sized kamacite particles, which are in a K–S or N–W relationship.

Electron microprobe analyses along line scans across kamacite and modified plessite show that the kamacite contains 6.3 0.1 wt% Ni and the taenite particles in the

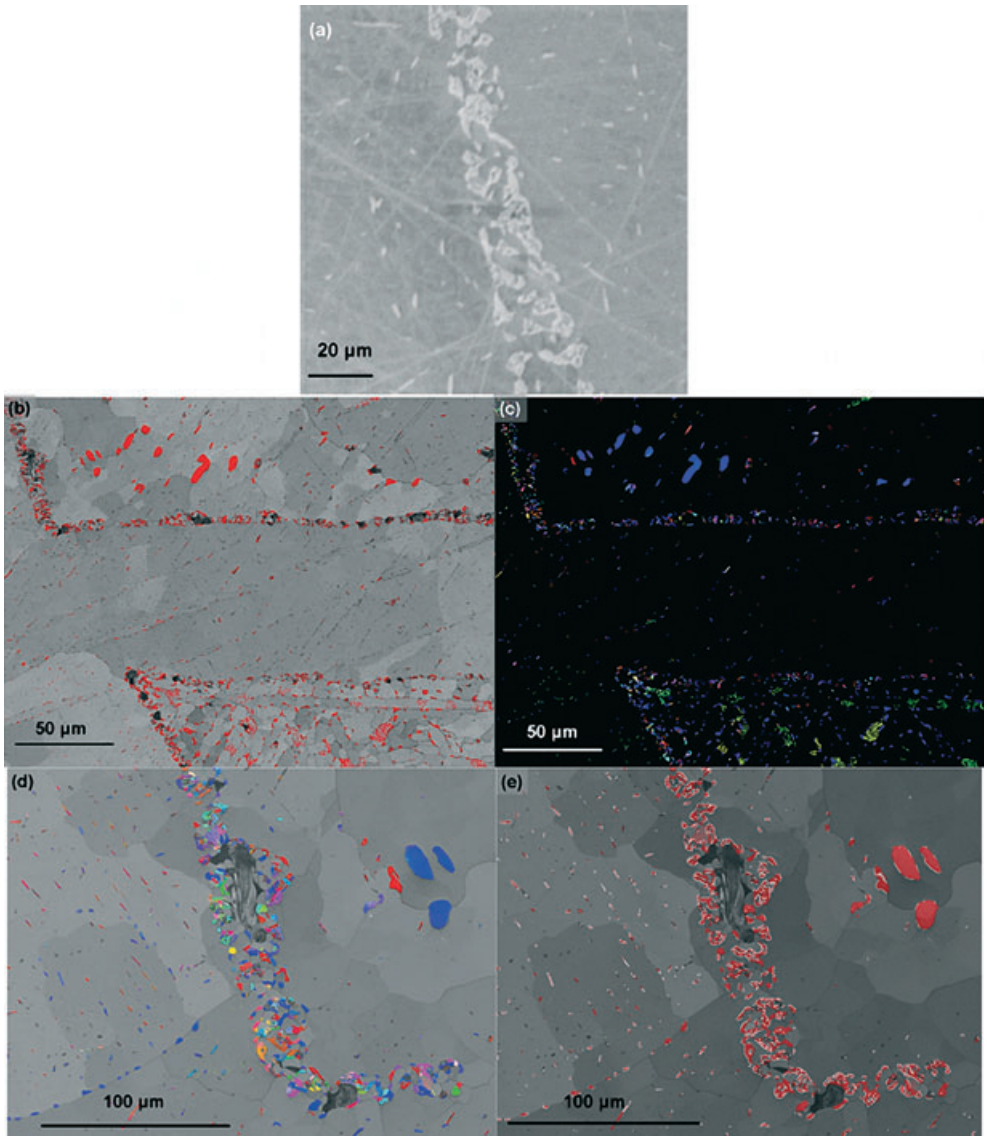

Fig. 2. Microstructure of Maria Elena showing effects of reheating. a) Backscattered electron photograph showing a band of spheroidized taenite particles (white) between two kamacite plates (gray) and smaller taenite laths, which precipitated in kamacite. b) Band contrast and fcc orientation map showing taenite (red) and partly recrystallized kamacite (gray) in two plessite fields adjacent to kamacite plates. c) Fcc orientation map of region in (b) showing taenite grains with diverse orienations and colors. d) Higher magnification band contrast and fcc taenite (colored) orientation map showing spheroidized taenite grains with diverse colors and orientations surrounded by recrystallized kamacite (gray). Taenite grains are also observed within the surrounding recrystallized kamacite grains and on grain boundaries. e) Band contrast map of the region in (d) with fcc taenite in red. Grain boundaries between kamacite and taenite that have K–S or N–W orientation relationships between their close-packed planes are marked by white lines.

plessite, many of which show internal kamacite precipitates, and have diverse compositions averaging 22.9 7.5 wt% Ni (Table 4). To determine the composition of the phases that could not be resolved because of the nominal 1 μm diameter resolution of the electron microprobe, FIB sections 50–100 nm in thickness of taenite-rich regions in Maria Elena were prepared for the AEM. This technique can obtain composition

Table 3. Kurdjumov–Sachs (K–S) and Nishiyama–Wassermann (N–W) orientation relationships between fcc γ austenite and bcc α ferrite (kamacite or α_2 martensite).

Orientation	Plane	Direction
K–S	$\{111\}_\gamma \supseteq \supseteq \{110\}_\alpha$	$<1\text{-}10>_\gamma \supseteq \supseteq <1\text{-}11>_\alpha$
N–W	$\{111\}_\gamma \supseteq \supseteq \{110\}_\alpha$	$<0\text{-}11>_\gamma \supseteq \supseteq <001>_\alpha$

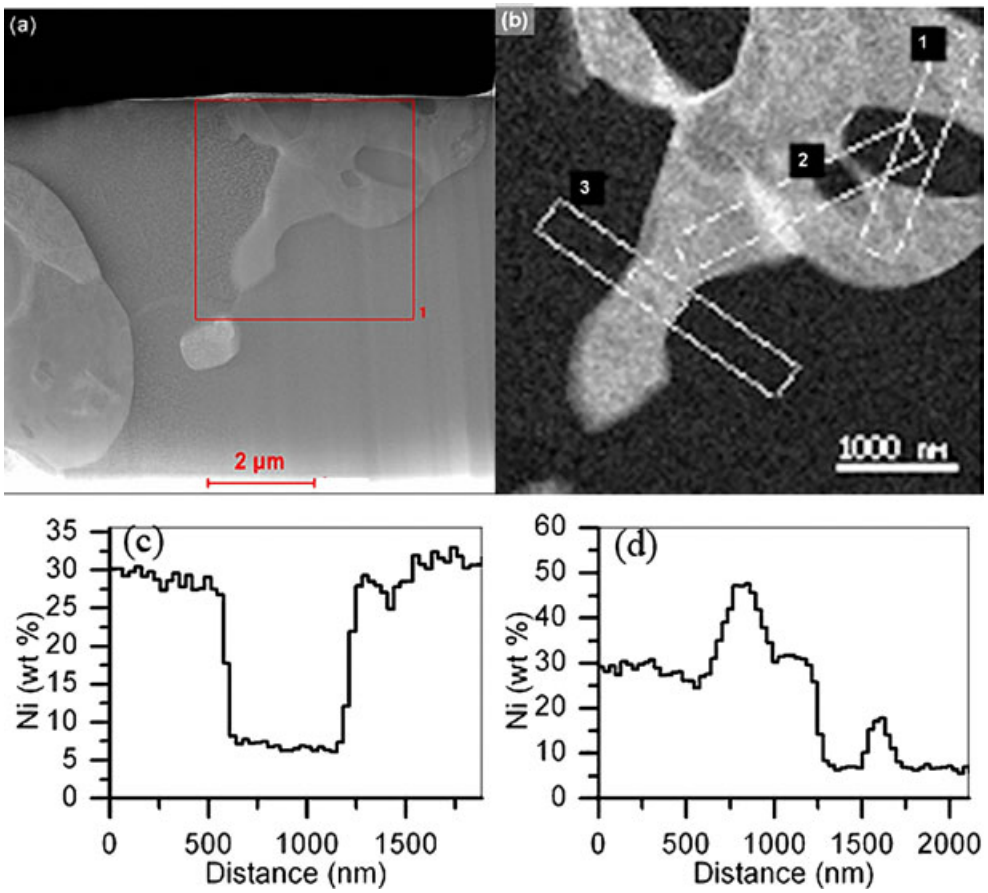

Fig. 3. a) Annular dark field STEM photo of Maria Elena showing taenite (light gray) and kamacite (dark gray). b) Ni concentration map of the 4 ∩ 4 μm region in (a) showing kamacite particles within high-Ni taenite (white). The X-ray scan was 125 ∩ 125 pixels, 32 nm pixel^{-1}. c,d) Two Ni concentration profiles measured across taenite (25–45% Ni) and kamacite (6–7% Ni). The positions of these profiles are marked 1, 2 in (b). The high Ni concentration in profile 2 in (d) is due to enhanced grain boundary diffusion.

Table 4. Average Ni concentrations determined using EPMA in kamacite, taenite particles (including kamacite microprecipitates) and phosphide, and kamacite–taenite equilibration temperatures.

Meteorite	Kamacite (σ, wt%)	Taenite (σ, wt%)	Phosphide (σ, wt%)	K–T equilibration temperature (σ, °C)
Maria Elena	6.3 0.1	22.9 7.5	N⊇A	570 60
Hammond	5.7 0.6[a]	23.2 1.1[a]	13.4–22.8[b]	520 10
	6.3 0.2[c]	24.2 2.2[c]		
Ternera	7.2 0.1	26.4 4.1	38.0	510 30
Fuzzy Creek	6.9 0.1	26.2 2.8	36.7	510 20
Babb's Mill (Blake's Iron)	6.9 0.3	31.3 5.1	N⊇A	500 40
Babb's Mill (Troost's Iron)	7.0 0.1	25.8 3.1	33.7	510 20

Note: N⊇A = No phosphide observed.
[a]In original WidmanstÌtten kamacite (coarse-grained) region.
[b]Ni variation in one 13 μm sized phosphide.
[c]In original plessite (fine-grained) region.

measurements in regions as small as 2 nm. Figure 3a shows an annular dark field STEM photo of a thin section containing a taenite particle, which has several internal kamacite crystals. The Ni concentration map of a 16 μm^2 area of this sample is shown in Fig. 3b. Composition profiles were measured across taenite-kamacite interfaces in the taenite particles (Figs. 3c and 3d). In these scans, which have a resolution of 32 nm pixel^{-1}, the taenite

Table 5. Ni concentrations in kamacite and taenite obtained from STEM analysis of FIB samples and kamacite–taenite equilibration temperatures.

Meteorite	Kamacite (wt%)	Taenite Min. Ni[a] (wt%)	K–T equilibration temperature (°C)	Taenite Max. Ni[b] (wt%)
Maria Elena	6 1	28–30	520 10[c]	> 45
Hammond	6 1	35–40	400 20[d]	40
Ternera	6 1	25–30	500 20[d]	> 40
Fuzzy Creek	7 1	25 3	500 20[d]	> 35
Babb's Mill (Blake's Iron)	6.0 0.5	27 2	530 20[c]	40
Babb's Mill (Troost's Iron)	6 1	28 1	500 10[d]	40

[a]Minimum measured at or near the center of the taenite grain; 1–4 taenite grains analyzed per meteorite.
[b]Maximum Ni in taenite at taenite-kamacite boundary or taenite–taenite grain boundary.
[c]Determined using Fe-Ni phase diagram (phosphide absent).
[d]Determined using Fe-Ni-P phase diagram (phosphide present).

showed a rather uniform concentration of 28–30 wt% Ni (except for one region in Fig. 3d) and the kamacite contained 6 1 wt% Ni (Table 5). The Ni enrichment up to 45% Ni shown in scan 2 in Fig. 3d is attributed to Ni diffusion along a taenite–taenite grain boundary. A second FIB section that was scanned with a resolution of 2 nm pixel^{-1} showed Ni increases in taenite at boundaries with kamacite up to 45 wt%.

Hammond (Ungrouped)

Etched slices of Hammond show a somewhat indistinct and distorted WidmanstÌtten pattern of a medium octahedrite (Fig. 4a) (Buchwald 1975). At the micrometer scale, the microstructure is quite unlike that of a normal slow-cooled iron, as it consists of grains of kamacite, taenite, and schreibersite, which are 1–100 μm across (Fig. 4b). The regions that were once WidmanstÌtten kamacite plates appear in EBSD bcc orientation maps as coarse-grained recrystallized kamacite with grain sizes of mostly 20–100 μm (Fig. 4c). Some regions (e.g., the large red region in Fig. 4c) appear to be millimeter-sized remnants of the original kamacite plates. Taenite crystals approximately 3–6 μm in size (some with embedded submicrometer kamacite particles) are present on the coarse-grained recrystallized kamacite grain boundaries (Figs. 5a and 5b).

The regions between the kamacite plates that were originally plessite fields, now consist of fine-grained recrystallized kamacite with grain sizes of 10–20 μm plus a similar number of taenite crystals approximately 3–6 μm in size. These taenite crystals are located on the kamacite grain boundaries and contain submicrometer kamacites (Figs. 5c and 5d). EBSD maps show clearly that the fine-grained regions contain much higher abundances of taenite than the coarse-grained regions (Figs. 4d, 5c versus 5a). Both coarse and fine-grained regions also contain 1–5 μm wide schreibersite grains on the recrystallized kamacite grain boundaries (Figs. 5a and 5c). In the regions that were once kamacite plates, taenite grains show diverse orientations. Nearly all taenite grains are in a K–S or N–W orientation relationship (Table 3) with an adjacent kamacite grain.

Electron microprobe analysis shows that the phases in the coarse- and fine-grained regions have relatively similar compositions. Kamacite in coarse regions is more heterogeneous, and contains 5.7 0.6 wt% Ni, whereas fine-grained kamacite contains 6.3 0.2 wt% Ni (Table 4). The average Ni concentration of the 3–6 μm wide taenite–kamacite particles in the coarse-grained regions is 23.2 1.1 wt% Ni and in fine-grained regions, 24.2 2.2 wt% Ni (Table 4). Most phosphides are too small for accurate microprobe analysis, but one large phosphide approximately 13 μm across is unlike similar sized grains in normal slow-cooled irons, as it is chemically zoned from 13 wt% Ni near the center to 23 wt% at the phosphide–kamacite boundary.

Composition profiles taken from a Ni X-ray STEM image with a resolution of 32 nm pixel^{-1} showed that taenite contained 35–40 wt% Ni, and kamacite 6 1 wt% Ni (Table 5). As X-ray scans with a resolution of 2 nm pixel^{-1} were not made, we cannot exclude the possibility that there are Ni increases in taenite at taenite–kamacite and taenite–taenite boundaries at the nanometer scale, as observed in Maria Elena.

Ternera (IVB)

Ternera has the chemical composition of a high-Ni IVB member with 17.6% Ni (Rasmussen et al. 1984; Walker et al. 2008). However, it completely lacks the microstructure of other high-Ni IVB irons like Weaver Mountains, which have oriented kamacite platelets and grains up to 20 μm in width with numerous 5–10 μm phosphides in kamacite set in a submicrometer plessite matrix (Buchwald 1975; Yang et al. 2010). Instead Ternera has a coarser microstructure consisting of polycrystalline mixture of roughly equant kamacite and taenite grains (Fig. 6a), and minor amounts of phosphide $(Fe\text{-}Ni)_3P$. The kamacite and taenite grains

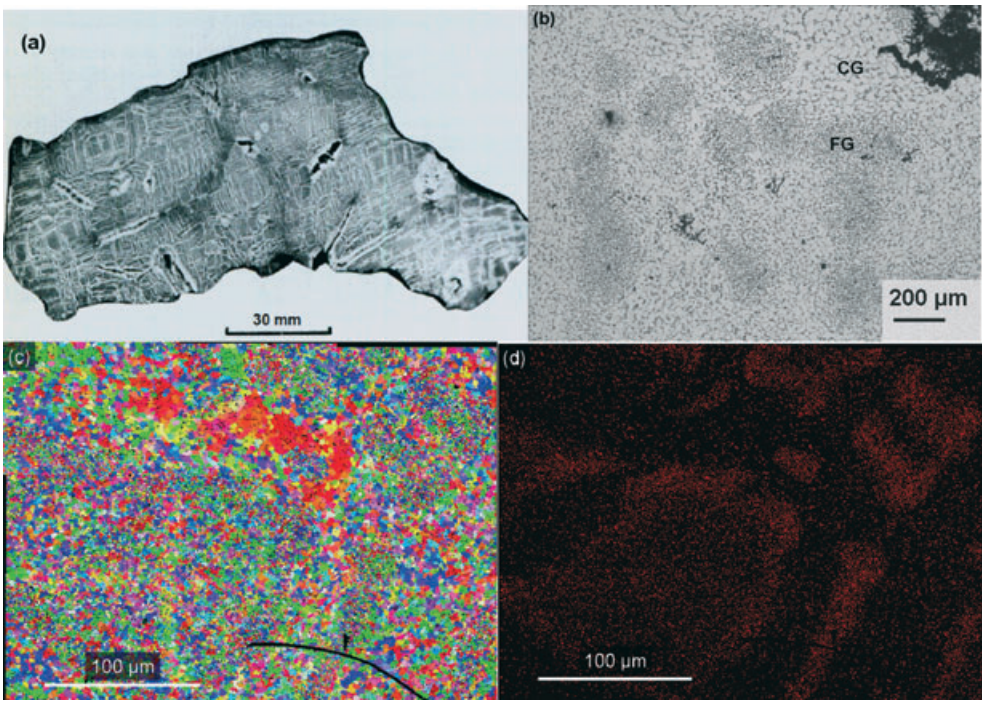

Fig. 4. a) Etched slice of the Hammond ungrouped iron showing a distorted and somewhat indistinct Widmanstὶtten pattern (from Buchwald 1975, fig. 836, used by permission of Arizona State University). b) Optical photomicrograph showing fine-grained regions, which were originally plessite, and coarse-grained regions, which were originally kamacite plates. c) EBSD bcc orientation map of coarse and fine-grained regions showing kamacite grains with diverse colors and orientations. The tiny black grains are taenite. d) EBSD map showing fcc taenite region in (c). The fine-grained regions contain much higher abundances of fcc taenite (red).

are mostly 5–10 μm in size and kamacite is almost twice as abundant as taenite.

Electron-probe microanalysis showed that kamacite contained 7.2 0.1 wt% Ni and taenite grains with micrometer-scale kamacite particles having average Ni concentrations of 26.4 4.1 wt% (Table 4). Figures 6b and 6d show EBSD maps of the fcc and bcc phases, respectively; both phases are oriented in diverse orientations. The micrometer-scale kamacite particles within the taenite particles have a K–S or N–W orientation relationship along close-packed planes with the fcc phase (Table 3; Fig. 6c). In addition, portions of the boundaries between the 5–10 μm kamacite and taenite particles also show a mutual K–S or N–W relationship. Phosphide particles, 1–7 μm in size, are observed at kamacite and taenite phase boundaries as shown in Figs. 6b–d). The composition of one large (~5 μm) phosphide is 38.0 wt% Ni and 15.4 wt% P (Table 4).

Figure 7a shows an annular dark field TEM photo of a FIB thin section of a taenite particle in Ternera containing numerous kamacite precipitates. The Ni concentration variation in a 4 ∩ 4 μm region in Fig. 7a is shown by the color scanning X-ray picture in Fig. 7b with a resolution of 32 nm pixel^{-1}. The kamacite precipitates have about 7 wt% Ni as shown by the dark blue color on the Ni X-ray scanning picture. The taenite Ni concentration varies from 25 to 40 wt% with the highest Ni concentration occurring along what appears to be a grain boundary between taenite crystals. Another FIB thin section of a Ternera taenite particle with kamacite precipitates was examined at higher resolution of 2 nm pixel^{-1}. Compositional profiles across approximately 200 nm wide taenite regions show "M-shaped" Ni profiles typical of Widmanstὶtten pattern formation with about 25 wt% Ni in the center and 35–40% Ni at the kamacite interface. The submicrometer kamacite contains 6 wt% Ni.

Fuzzy Creek (IVA)

Fuzzy Creek is a high-Ni IVA iron with 11.8% Ni that lacks the expected fine octahedral structure of IVA irons (Malvin et al. 1984). The kamacite matrix shows a recrystallized structure with a grain size of 5–20 μm. Taenite grains, which are 2–10 μm in size and contain smaller kamacite precipitates, are distributed on grain boundaries together with a smaller number of schreibersite grains 1–2 μm in size (Fig. 6) (McCoy et al. 2011). Kamacite analyzed using EPMA contains 6.9 0.1 wt% Ni (Table 4) and the Ni concentration of the taenite–kamacite particles ranges from ~22 to ~32 wt% Ni with an average Ni content of

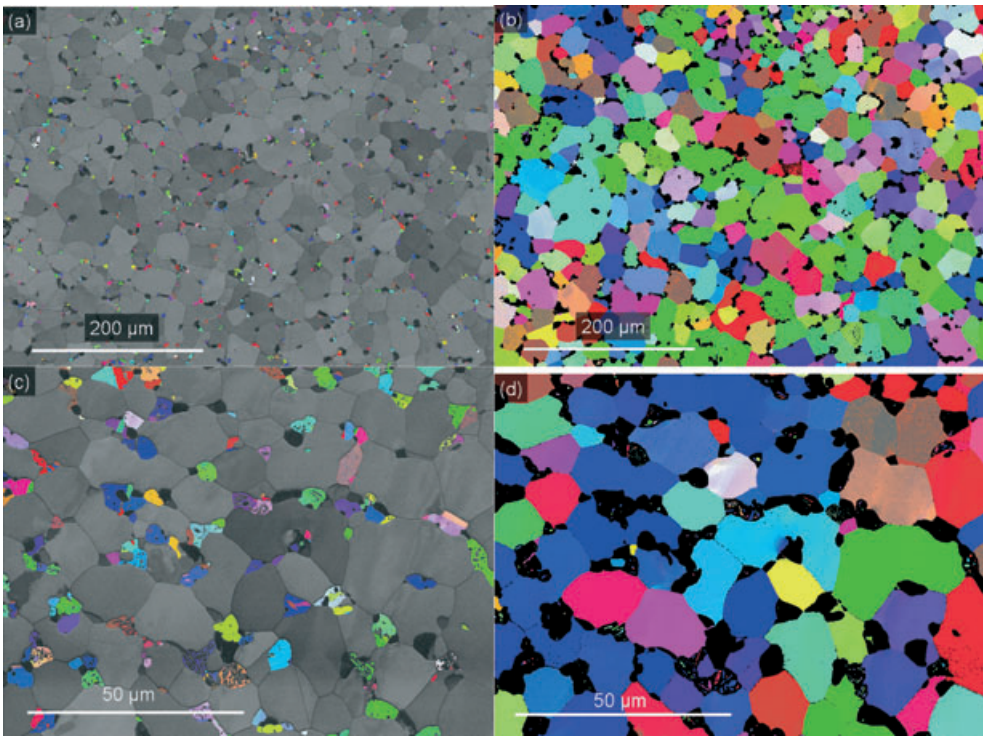

Fig. 5. EBSD images of taenite and kamacite in coarse-grained regions, which were originally kamacite plates, (a-b) and fine-grained regions, which were originally plessite, (c-d) in the Hammond meteorite. a,c) Combined band contrast and fcc orientation maps showing taenite grains with diverse colors and orientations and black phosphides on the grain boundaries of polycrystalline kamacite (gray). Some kamacite is present in the taenite grains. b,d) Bcc orientation maps showing kamacite grains with diverse orientations and colors. The predominance of green grains in (b) and blue-purple grains in (d) indicates that the recrystallized grains are not randomly oriented, but retain some structural memory of the original kamacite crystals.

26.2 2.8 wt% Ni (Table 4). EPMA analysis of the largest schreibersite grain in our sample gives 36.7 wt% Ni, but the low P concentration of 13.8 wt% P suggests that the Ni content was higher, probably approximately 40% Ni. The bulk composition of Fuzzy Creek obtained from line scans using EPMA is 12.4 wt% Ni, and 0.18 wt% P (McCoy et al. 2011).

Electron backscattered diffraction maps show that taenite and kamacite grains in Fuzzy Creek both show diverse orientations (Figs. 8a and 8b). Taenite grains typically have a K–S or N–W {110}bcc ⊇ ⊇ {111}fcc orientation relationship with an adjacent recrystallized kamacite grain. Within single taenite grains, the kamacite precipitates show several different orientations (Fig. 8b). FIB thin sections of Fuzzy Creek were investigated using STEM and X-ray analysis, McCoy et al. (2011). Taenite grains contain 25 3 wt% Ni at their centers and >35 wt% at interfaces with kamacite. Kamacite contains 7 1 wt% Ni (Table 5).

Babb's Mill (Blake's Iron) (Ungrouped)

This ungrouped iron with 11.8 0.3 wt% Ni (Schaudy et al. 1972) shows no oriented kamacite plates or platelets (Buchwald 1975). Instead, it has a polycrystalline kamacite matrix with grains mostly 10–20 μm in size and approximately 15 vol% taenite (Fig. 9). Taenite grains, which are 5–20 μm in size and contain small kamacites, are located on kamacite grain boundaries. No phosphide was observed, consistent with the low bulk P content (0.02 wt%). From EPMA measurements, the average Ni content of kamacite is 6.9 0.3 wt%, and the bulk Ni content of the taenite–kamacite particles is 31.3 5.1 wt% (Table 4).

A FIB section of a kamacite–taenite region intergrowth was analyzed. The central part of the taenite contains 27 2 wt% Ni, and at the kamacite interface, it contains 40 wt% Ni (Table 5). Kamacite within 250 nm of the kamacite–taenite interface contains 6 0.5 wt% Ni and shows a small decrease near the interface. No EBSD data are available for this iron.

Babb's Mill (Troost's Iron) (Ungrouped)

This ungrouped iron with 17.7 wt% Ni (Scott et al. 1973) displays two different microstructures: one that was produced by reheating before impact with the Earth, and the second that was produced by a blacksmith (Buchwald

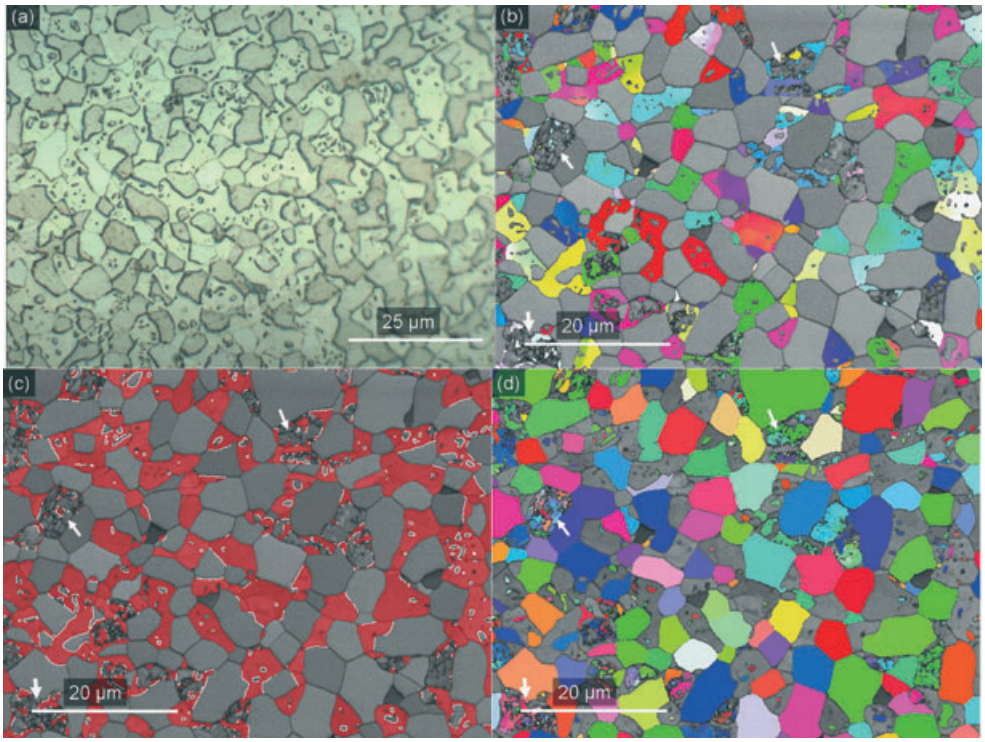

Fig. 6. Microstructure of the Ternera iron meteorite. a) Reflected-light photomicrograph of etched section showing kamacite (darker regions) and taenite (lighter regions). Small kamacite particles are observed within some of the taenite phases. b–d) EBSD images of another region. b) Combined band contrast and fcc orientation map showing taenite grains with diverse colors and orientations and polycrystalline kamacite (gray). c) Band contrast image with fcc taenite in red and K–S or N–W boundaries between kamacite and taenite marked in white. d) Combined band contrast and bcc orientation map showing bcc kamacite with diverse colors and orientations. Small bcc kamacite particles are also present in the fcc taenite (gray phase). Bcc regions marked by white arrows are probably martensite (see the Discussion section). Particles that appear dark gray in (b), (c), and (d) are phosphides.

1975). However, for reasons that are discussed in the Appendix, we infer that the Babb's Mill (Troost's Iron) sample, that Buchwald (1975) took to be an unforged sample, was actually mislabeled. In the Appendix, we also discuss the history of both Babb's Mill meteorites and the thermal history and microstructure of the mistreated sample of Babb's Mill (Troost's Iron). The unforged sample of Babb's Mill (Troost's Iron) that we analyzed using SEM, EPMA, and STEM, and described below is ASU 2905.

Babb's Mill (Troost's Iron) is closely related in composition to South Byron and ILD 83500 (Wasson et al. 1989). However, Babb's Mill (Troost's Iron) displays a polycrystalline intergrowth of kamacite and taenite rather than the ataxitic structure of South Byron (Buchwald 1975) or the high-Ni IVB irons. Kamacite is twice as abundant as taenite, and both phases have particle sizes of 5–10 μm (Fig. 10a), as in Ternera, which has a similar microstructure (Fig. 6a; Table 1). The average Ni contents from EPMA are 7.0 0.1 wt% for kamacite, and 25.8 3.1 wt% for taenite grains (Table 4). The large variation in taenite Ni content is due to the presence of micrometer-sized kamacite. Fe, Ni, and P scanning X-ray maps produced with the EPMA show the presence of 2 μm sized phosphides at kamacite–taenite interfaces. An attempt to analyze the largest phosphide gave 33.7 wt% Ni, and 10.2 wt% P. As schreibersite contains 15.5 wt% P, the actual Ni content is probably >35 wt% (Table 4).

Electron backscattered diffraction maps show that bcc kamacite and fcc taenite are present in numerous different orientations (Figs. 10b and 10c), and at many boundaries they show a K–S or N–W orientation relationship. In addition, almost all the micrometer-sized kamacites within the taenite grains have a K–S or N–W orientation relationship with the surrounding fcc phase. Most of the taenite grains contain approximately 5–20 vol% of small kamacite precipitates, but a few of the larger grains have higher concentrations of bcc phase. This bcc phase is probably martensite as discussed below.

Figure 11a shows an annular dark field STEM image from the AEM of a taenite region containing kamacite particles surrounded by kamacite grains in Babb's Mill (Troost's Iron). The Ni variation in a 1 μm^2 area of the

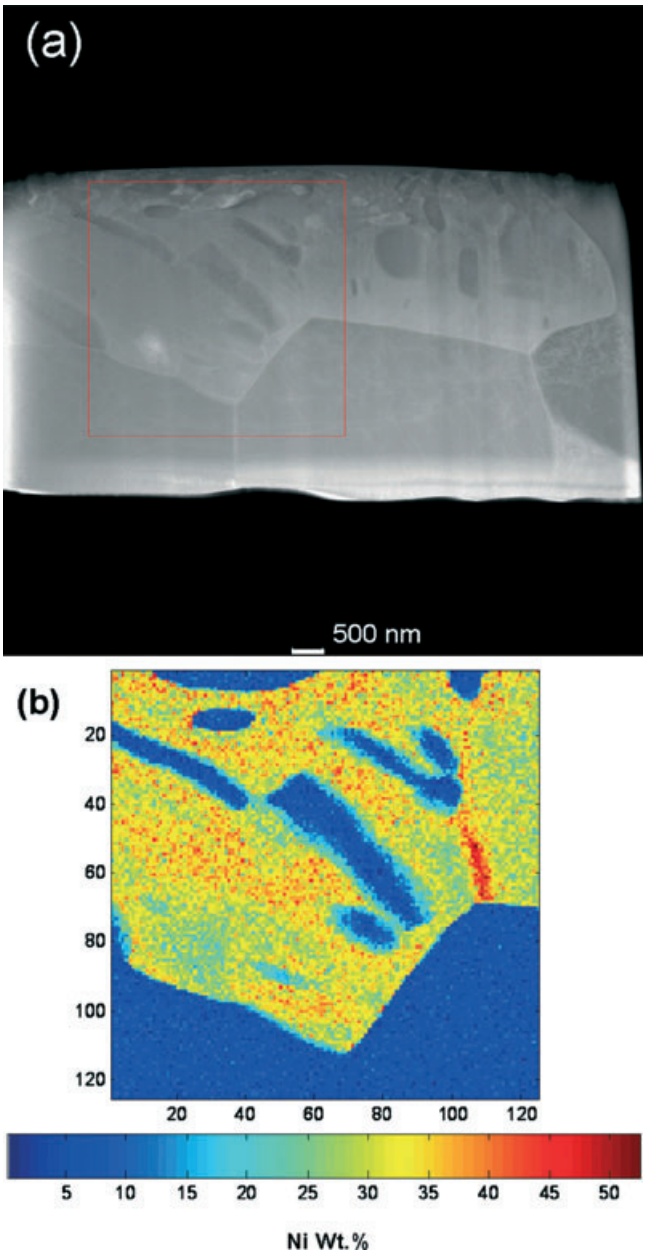

Fig. 7. STEM analysis of a taenite particle in the Ternera iron meteorite. a) Annular dark field STEM photo of a taenite particle (light) containing small kamacite regions (dark). b) Ni variation in the 4 ∩ 4 μm region shown in (a). X-ray scan size is 125 ∩ 125 pixels, 32 nm pixel^{-1}. The quantitative Ni scanning X-ray map shows several kamacite precipitates, which are dark blue, indicative of Ni contents approximately 5–7 wt %. Regions of red and yellow taenite, which have Ni contents of 28 to >35 wt% Ni, are very probably taenite, whereas regions of light green, which have Ni contents below 28 wt% Ni, are very probably martensite (see the Discussion section).

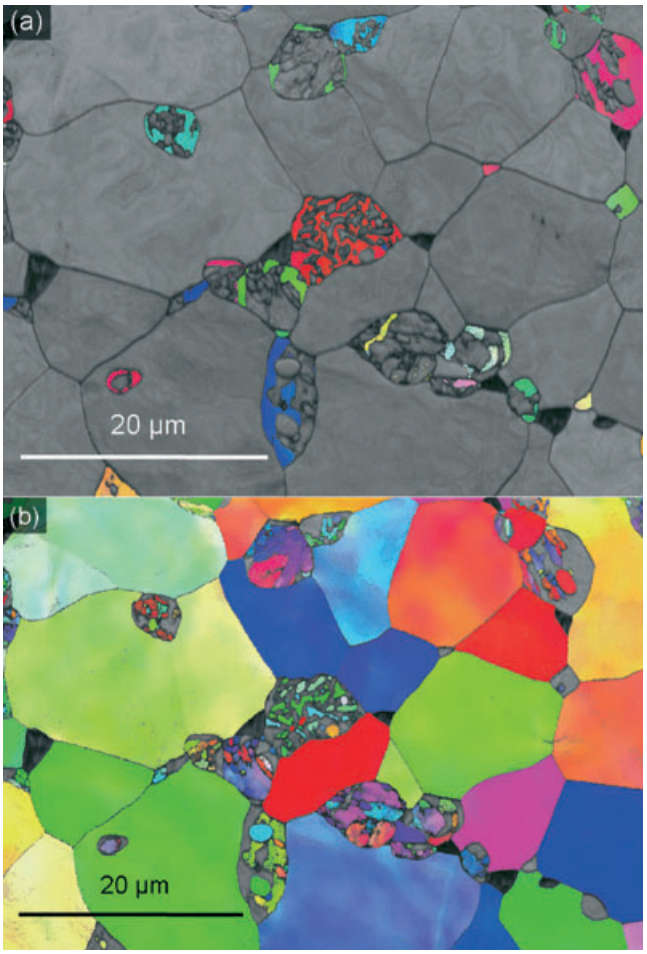

Fig. 8. Microstructure of the Fuzzy Creek iron meteorite. a) Combined EBSD band contrast and fcc orientation map showing taenite grains with diverse colors and orientations, polycrystalline kamacite (gray), and phosphide (black). b) EBSD orientation map showing bcc kamacite grains with diverse colors and orientations and taenite (gray). Bcc phase is also present in the fcc taenite regions as kamacite precipitates and martensite α_2 with ∪28 wt% Ni (see the Discussion section). The black regions at kamacite triple boundaries are phosphides.

taenite microstructure (Fig. 11a) is shown in Fig. 11b. The interior of the particle, the taenite matrix, contains about 28 1 wt% Ni as shown by Ni profiles 1 and 5 (Figs. 11c and 11d; Table 5). The Ni content of the taenite increases at kamacite–taenite interfaces up to 40 wt% Ni (Fig. 11c), and at taenite–taenite boundaries up to 45 wt % Ni using grain boundary diffusion (from profile 2 in Fig. 11b). Kamacite at the taenite–kamacite boundary has about 6 1 wt% Ni. Small kamacite precipitates with about 6 wt% Ni are present in the taenite particles as observed by the Ni composition profile across a small approximately 30 nm kamacite particle (Fig. 11d).

DISCUSSION

To determine the thermal history of the reheated irons and the reheating mechanism, we need to reconstruct the primary structure, how it was modified

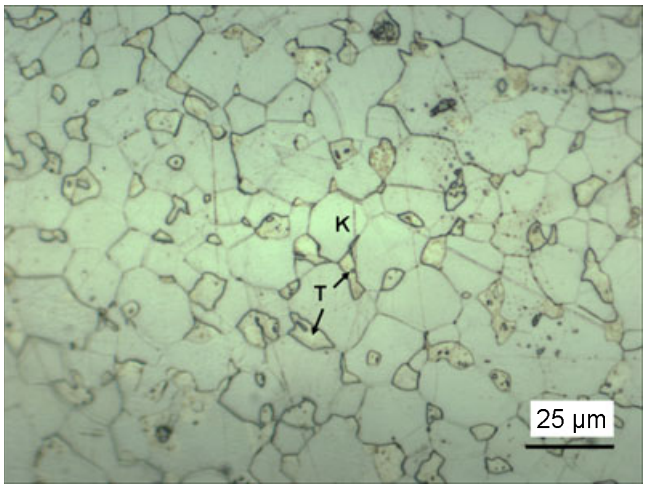

Fig. 9. Microstructure of Babb's Mill (Blake's Iron). Reflected-light photomicrograph of an etched section showing particles of taenite (T) on grain boundaries in kamacite (K). The taenite particles contain small kamacite precipitates.

during reheating, and what happened during subsequent cooling. We make use of the record preserved in kamacite, taenite, and phosphide that is revealed by EBSD as well as more conventional data obtained using SEM, scanning X-ray microanalysis, and optical techniques. First, however, we need to understand the role of martensite formation.

Microstructure of Reheated IronsöMartensite

In slowly cooled irons (as well as metal in ordinary chondrites, pallasites, mesosiderites, etc.), the bcc phase (called α by metallurgists), is kamacite with $<7\%$ Ni. The fcc phase (γ) is taenite, which is much richer in Ni and borders kamacite in the WidmanstÌtten pattern or is a major component of plessite. On cooling, taenite develops an M-shaped Ni profile as kamacite continues to increase in size as shown by the Fe-Ni phase diagram (Fig. 12). Metastable taenite that contains $\sim$10 to $\sim$28 wt% Ni starts to transform to martensite α_2, as it cools below M_s, the martensite start temperature. Martensite, which has a distorted bcc structure, forms by a shear transformation below the M_s temperature, which ranges from 500 °C for taenite with approximately 10 wt % Ni to room temperature for taenite with approximately 28 wt% Ni (Fig. 12).

In slowly cooled meteorites, martensite transforms on further cooling to plessite, a micrometer- or submicrometer-sized intergrowth of bcc kamacite and fcc taenite, the equilibrium phases (Zhang et al. 1993; Reisener and Goldstein 2003; Goldstein and Michael 2006; Goldstein et al. 2009). However, in reheated irons, which cooled faster, there may be insufficient time for martensite to decompose. In this case, the central regions of fcc taenite grains with M-shaped Ni profiles could contain martensite with Ni concentrations as high as approximately 28% Ni. As diffraction patterns from the kamacite, bcc α, and martensite, distorted bcc α_2, structures that are identical in EBSD, kamacite, and martensite would appear on bcc Fe-Ni orientation maps. Below, we combine information from EBSD, which allows bcc and fcc Fe-Ni to be identified from their electron diffraction patterns, SEM, scanning X-ray microanalysis, and optical techniques to show that high-Ni martensite is present in the reheated irons.

Table 4 shows that the mean Ni concentration in taenite particles determined using EPMA with approximately 1 μm resolution is about 25% for all the six irons except Babb's Mill (Blake's Iron). This composition and that of kamacite suggest that these meteorites equilibrated at approximately 510 °C, well above the martensite start temperature of approximately 100 °C for taenite of this composition (Fig. 12). Table 5 lists the minimum Ni concentrations in taenite in the six irons determined using AEM at resolutions of approximately 2 nm at or near the center of small micrometer-sized taenite particles. These Ni contents vary from 25 to 30 wt% except for Hammond, which has higher Ni contents. As the inner portions of some of the taenite particles have $<\sim$28 wt% Ni, bcc regions of martensite should be present unless they have decomposed.

The fcc and bcc orientation maps for Ternera (Figs. 6b and 6d) provide strong evidence for the existence of martensite, α_2. Most of the fcc particles in Ternera consist of a single fcc crystal that contains a few vol% of micrometer-sized bcc precipitates of kamacite (Fig. 6b). A second type of composite bcc–fcc particle consists of a skeletal fcc single crystal that partly encloses a much larger volume of bcc Fe-Ni (three examples are indicated by white arrows in Figs. 6b–d). These bcc regions appear darker gray in the band contrast images than the 5–10 μm bcc kamacite crystals because of numerous internal black grain boundaries (Fig. 6b). Figure 6c shows that both types of composite particles may show K–S or N–W orientations with an adjacent kamacite grain.

We could not analyze the composition of the dark gray bcc regions in Figs. 6b and 6c, but our AEM studies of other taenite grains suggest strongly that the dark gray regions are martensite with approximately 25–28% Ni. Figure 7a shows an annular dark field image of a typical 10 μm wide taenite particle with kamacite precipitates in Ternera. The quantitative Ni X-ray scanning map of this particle (Fig. 7b) shows regions with approximately 25–28 wt% Ni (light green), which are very probably martensite. Ni profiles across a second

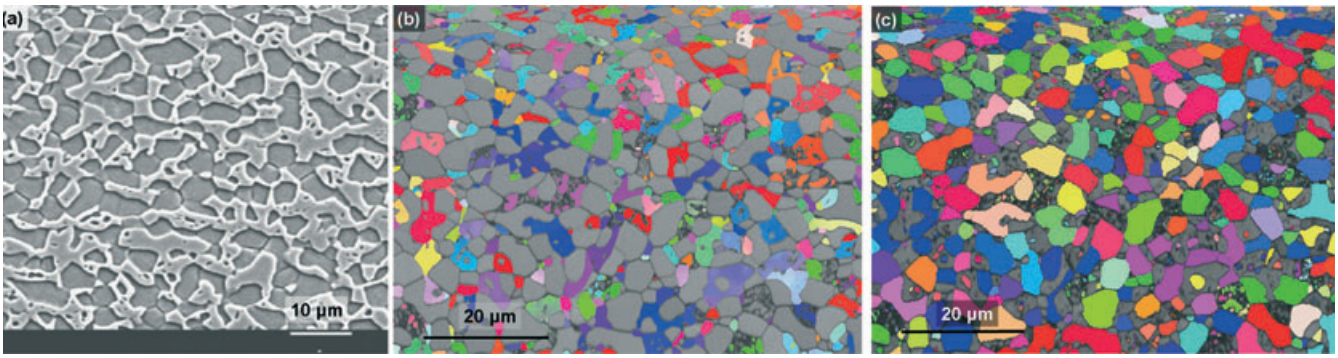

Fig. 10. Microstructure of Babb's Mill (Troost's Iron) specimen ASU 2905. a) Secondary electron image showing kamacite (dark gray matrix) and taenite (light gray) with inclusions of kamacite. Phosphides observed as small bright grains are present at kamacite–taenite interfaces. b) Combined band contrast and fcc orientation map showing taenite grains with diverse colors and orientations and polycrystalline kamacite (gray). Bcc kamacite regions are also present within most of the taenite particles. A few small dark gray phosphides are observed at kamacite–kamacite grain boundaries. c) Combined band contrast and bcc orientation map of same region as (b) showing kamacite with diverse colors and orientations and taenite (gray). Kamacite precipitates with diverse orientations are present in many taenite particles.

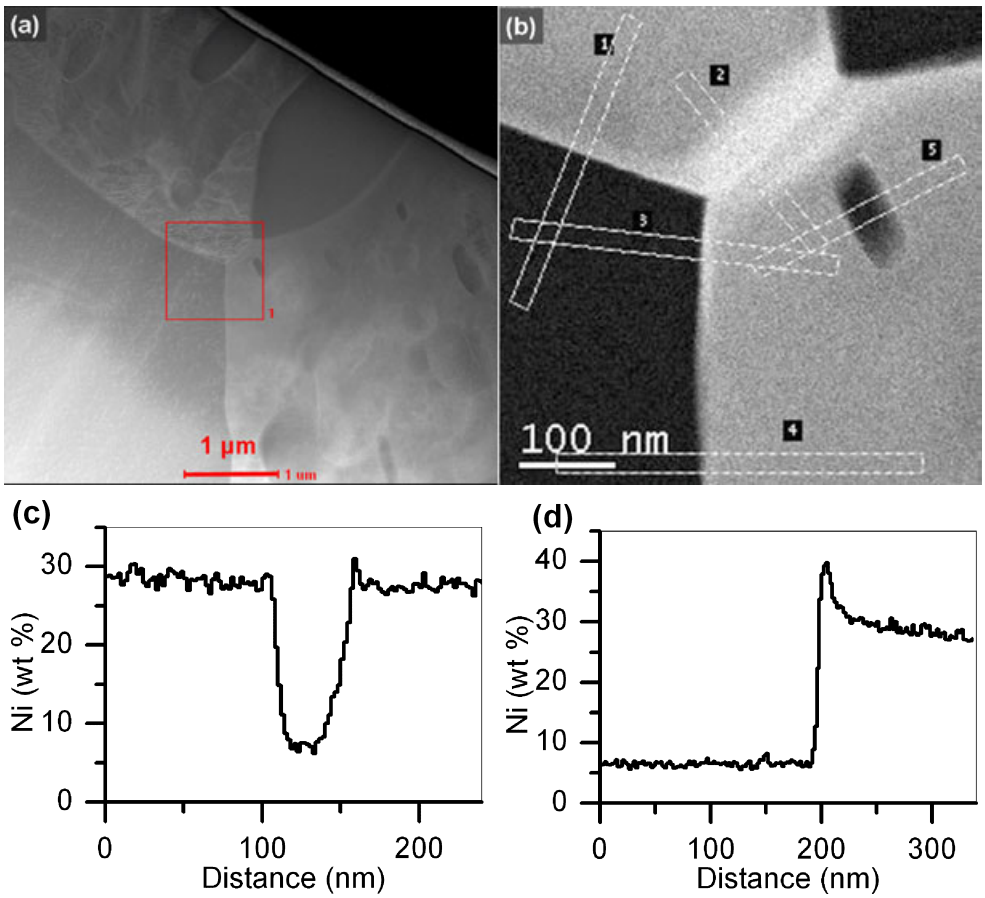

Fig. 11. STEM analysis of a taenite grain in the kamacite matrix of Babb's Mill (Troost's Iron) (ASU 2905). a) Annular dark field STEM image of a taenite grain at a kamacite–kamacite grain boundary containing kamacite precipitates. b) Ni X-ray map of a 1 μm^2 area of the taenite grain shown in (a). Scan is 250 ∩ 250 pixels, 2 nm $pixel^{-1}$. c) Ni composition variation across a small 30 nm wide kamacite precipitate. (Scan path 5 shown in b.) d) Ni composition profile across a kamacite–taenite boundary. (Scan path 1 shown in b.)

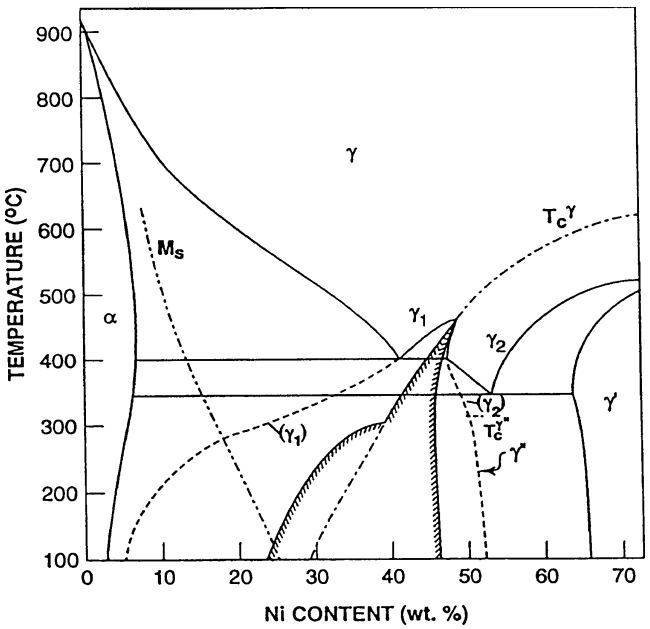

Fig. 12. Fe-Ni binary phase diagram (Yang et al. 1996). α is a low-Ni bcc phase, γ a high-Ni fcc phase, γ_1 a low-Ni paramagnetic fcc phase, γ_2 a high-Ni ferromagnetic fcc phase, γ′ is ordered Ni_3Fe, γ′ is ordered FeNi tetrataenite, and M_s is the martensite start temperture. T_c^γ is the Curie temperature of the γ phase. $T_c^{\gamma'}$ is the ordering temperature of FeNi, γ′.

taenite particle with kamacite precipitates at a higher resolution confirm that there are regions with 25–28 wt % Ni, which probably transformed to martensite.

We conclude from the EBSD and quantitative Ni analyses of Ternera that the darker gray bcc regions in Figs. 6b and 6c are largely composed of martensite containing 25–28 wt% Ni. The adjacent skeletal taenite regions mostly contain >28 wt% Ni. Similar occurrences of martensite in taenite particles can be identified in the EBSD images of Fuzzy Creek (Figs. 8a and 8b) and Babb's Mill (Troost's Iron) (Figs. 10b and 10c). Only a few occurrences of martensite are observed in Hammond (Figs. 5c and 5d) consistent with the higher Ni content in taenite (Table 5). We believe that these occurrences of martensite, α_2, are the first documented examples of untransformed martensite in iron meteorites.

Thermal History of Reheated Irons

Taenite Compositions and Kamacite–Taenite Equilibration Temperatures

Before we discuss the thermal history of each iron, we can take advantage of our measurements of the Ni content in kamacite and taenite using EPMA (~1 μm spatial resolution) and AEM (up to 2 nm spatial resolution) to obtain equilibration temperatures for each meteorite. These equilibration temperatures are also related to the cooling rate of the reheated irons as described in this section. Although the taenite grains in the reheated iron meteorites are only 2–20 μm in size (Table 6), their Ni concentrations are crucial to understanding the thermal histories of the irons. Their compositions were measured using both EPMA of polished samples and EDS X-ray analysis of FIB prepared thin foils in the STEM (Tables 4 and 5). The EPMA data give the average composition of particles that were 5 μm or larger and commonly contained smaller kamacite grains, which grew inside taenite (Figs. 2a, 5c, 5d, 6, 8, 9, 10b, and 10c). The large variations in average Ni in taenite (Table 4) for each meteorite are due to the variability of the amount of kamacite in the taenite particles under the electron beam. We believe that the average compositions of taenite particles and kamacite (Table 4) are accurate, as they are consistent with the volume percent of the phases that we measured and the bulk composition of the meteorites (Table 2).

The STEM–AEM analyses of taenite show relatively homogeneous Ni concentration profiles when measured at low resolutions of approximately 30 nm, but at resolutions of 2–4 nm, they typically show characteristic increases toward the kamacite interface (Fig. 11c). We infer that these Ni profiles reflect kamacite growth during cooling, and that Ni enrichments across taenite particles mark grain boundaries, which allow enhanced diffusion (Fig. 11b). Table 5 shows the minimum Ni at the center of the taenite and the highest Ni concentration at the edge of the taenite in contact with kamacite or at a taenite–taenite grain boundary.

The kamacite and taenite compositions represent an α + γ tie line at a specific temperature in the Fe-Ni or Fe-Ni-P phase diagram (Romig and Goldstein 1980). Meteorites containing phosphides are P saturated (Table 2) and follow ternary diagram α + γ tie lines, whereas those without phosphides follow the binary α + γ Fe-Ni tie lines. The equilibration temperatures inferred from the measurements of Ni in taenite (Tables 4 and 5) in the six meteorites are listed in Table 6. The equilibration temperatures inferred from the average and minimum Ni concentrations depend on the peak temperatures, cooling histories, and taenite grain sizes. The maximum Ni concentrations measured at the kamacite–taenite interface and the inferred lowest temperature at which taenite and kamacite were in equilibrium depend on the cooling rate and analytical resolution used to measure the Ni X-ray scans in the TEM.

In the following sections, we reconstruct for each iron the thermal history responsible for the observed microstructure. The six meteorites are discussed in the order of increasing amount of reheating.

Table 6. Kamacite and taenite grain sizes, kamacite–taenite equilibration temperatures, and peak reheating temperatures in the six reheated iron meteorites.

	Grain size (μm)		Equilibration temperature (°C)			
Meteorite	Kamacite	Taenite	Ave. Ni[a]	Min. Ni[b]	Max. Ni[c]	Peak temperature (°C)
Maria Elena	10–200	2–5	570	520	< 400	570–700
Hammond	10–20	3–6	520	400		600–750
Fuzzy Creek	5–20	2–10	510	500		> 650
Babb's Mill (Blake's Iron)	10–20	5–20	500	530	400	> 700
Ternera	5–10	5–10	510	500	400	> 700
Babb's Mill (Troost's Iron)	5–10	5–10	510	500	400	> 625

[a]Derived from EPMA of mean composition of taenite particles (Table 4).
[b]Derived from TEM analysis of taenite (Table 5).
[c]Derived from TEM analysis of taenite at kamacite interface (Table 5).

Maria Elena (IVA)

The original microstructure before reheating would have closely resembled that of the IVA iron, Bishop Canyon, for example. The larger spaces between the WidmanstÌtten plates of kamacite would have been filled with plessite fields framed by thin taenite-rich lamellae (e.g., fig. 2b in Goldstein et al. 2009). The 5–20 μm wide spaces between parallel WidmanstÌtten plates would have been occupied by taenite lamellae having M-shaped Ni profiles, 100 nm wide tetrataenite rims, and 1–2 μm wide cloudy taenite zones (see figs. 1d and 5a in Yang et al. 2008; Goldstein et al. 2009). Reheating caused kamacite plates to recrystallize forming new subgrains in deformed regions and taenite to precipitate on grain boundaries within grains and on Neumann bands. The original taenite lamellae and their M-shaped Ni profiles, tetrataenite rims, and cloudy taenite were greatly modified. The taenite lamellae were spheroidized forming rounded taenite particles embedded in fine-grained kamacite (Fig. 2). High-Ni taenite was very susceptible to recrystallization on heating because of the large surface area of the fine intergrowths that formed in taenite on cooling. (See, for example, the region between the kamacite plate and plessite in fig. 2b in Goldstein et al. 2009.)

Some of the taenite (fcc) particles in the border of the plessite in the EBSD image in Fig. 2c have the same color and orientation as the numerous taenite (fcc) grains in the center of the plessite field, and clearly retained the original taenite orientation. However, there are also other grains with diverse colors and orientations that formed by recrystallization and nucleation and growth in kamacite. Figure 2e shows that the most of the taenite grains in what was originally a taenite lamella are in K–S or N–W relationship with adjacent kamacite. We infer that some of the taenite inherited this relationship from the original microstructure, and the rest of the taenite acquired the K–S or N–W relationship as a result of nucleation on kamacite or martensite during recrystallization.

The recrystallization of kamacite and the recrystallization and spheroidization of narrow taenite lamellae clearly point to reheating to temperatures above 400 °C, the minimum necessary for recrystallization of kamacite, and below 700 °C, the temperature at which kamacite would have been transformed to taenite (austenite) (Fig. 12). Kamacite that is reheated between these temperatures would exsolve taenite, as its Ni concentration exceeds the kamacite solubility limits in the binary Fe-Ni phase diagram (Fig. 12). The K–S or N–W orientations of the taenite blebs and platelets in kamacite plates are consistent with their formation between 400 and 700 °C. During cooling to 400 °C, the taenite particles developed nanometer-scale M-shaped Ni profiles with edge Ni concentrations up to 45% and internal kamacite precipitates with K–S or N–W orientations.

No direct experimental studies of taenite precipitation during the reheating of supersaturated kamacite have been performed. However, taenite platelets have been grown by reheating supersaturated martensite, α_2, to temperatures from 300 to 700 °C in Fe-Ni and Fe-Ni-P alloys (Goldstein and Ogilvie 1965; Doan and Goldstein 1970; Romig and Goldstein 1980). In general, for Fe-Ni alloys of 12–15 wt% Ni, 2 μm sized taenite platelets are formed with reheating times of approximately 4 months at 600 °C and about 1 μm taenite platelets are formed with reheating times of approximately 9 months at 500 °C (Romig and Goldstein 1980). For Fe-Ni-P alloys, reheating times to produce taenite precipitates are shorter. As diffusion rates of Ni are higher in martensite, α_2, it is reasonable to assume that a taenite platelet of micrometer size will be formed in kamacite at approximately 570 °C in a minimum of a few years. We conclude that Maria Elena was reheated to 570–700 °C and then cooled over a period of a few years or longer (Table 6).

Hammond (Ungrouped)

The indistinct WidmanstÌtten pattern in Hammond (Fig. 4a) shows that before it was heated and deformed, it was probably a medium octahedrite containing large schreibersites that formed before the WidmanstÌtten

pattern like, for example, the Grant IIIAB meteorite. Heating and deformation in Hammond were more intense than in Maria Elena, as the relict Widmanstὶtten pattern is more deformed, the kamacite plates were more thoroughly recrystallized to smaller equiaxed grains, and the plessite fields lack narrow taenite-rich borders. Kamacite in the prior kamacite plates and plessite fields recrystallized to form equiaxed grains with diverse orientations. The taenite grains in the plessitic fine-grained regions in Hammond also have very diverse orientations (Fig. 5c), unlike taenite in normal plessite (Goldstein and Michael 2006). A significant fraction appears to have a direct crystallographic relationship with the recrystallized kamacite grains, as they show K–S or N–W orientations relative to a neighboring kamacite grain.

The existence of a millimeter-sized relict region of a kamacite plate (Fig. 4c) shows that Hammond was probably not heated above 750 °C, the temperature at which all the kamacite would have been converted to taenite. A lower limit for the peak reheating temperature is set by the central Ni concentration in the phosphide grain (Table 4). The Fe-Ni-P phase diagram (Romig and Goldstein 1980) shows that a phosphide with 13 wt% Ni would have been in stable equilibrium with kamacite and taenite at about 600 °C. The edge of the schreibersite, which has 23 wt% Ni, would have been in equilibrium with kamacite and taenite at around 550 °C. We can infer that cooling from 600 to 550 °C was more rapid than normally experienced by iron meteorites, as they do not contain chemically zoned phosphides (Clarke and Goldstein 1978). Kamacite exsolved in taenite during further cooling with K–S or N–W orientations and equilibrium between kamacite and taenite continued on the nanometer scale to at least temperatures below 400 °C as confirmed using STEM analysis of taenite.

We conclude that Hammond experienced reheating and deformation that were more intense than for Maria Elena. Peak temperatures were in the range 600–750 °C, and the meteorite cooled subsequently over years.

Fuzzy Creek (IVA)

Although the Ni concentrations reported for Fuzzy Creek differ somewhatö11.8 0.3% (Malvin et al. 1984), 11.1% (Wasson and Richardson 2001), and 12.4% (McCoy et al. 2011)öthere seems little doubt that its composition closely matches that predicted for a very high-Ni IVA iron. We should therefore expect that Fuzzy Creek was originally a fine octahedrite like Duel Hill (1854) with 100 μm wide schreibersites located on the kamacite plates (see Buchwald 1975). In that case, taenite would have surrounded the Widmanstὶtten pattern kamacite, and plessite would form between the taenite borders. However, unlike Maria Elena and Hammond, Fuzzy Creek lacks any trace of a Widmanstὶtten pattern in the distribution of kamacite and taenite grains. We infer that it was heated at temperatures above 650 °C, so that kamacite was completely converted to taenite and recrystallized, so that new grains up to 10 μm in size were formed with diverse orientations.

On cooling, phosphide would have formed just above 650 °C, according to the Fe-Ni-P phase diagram (Romig and Goldstein 1980), at taenite grain boundaries. Kamacite formed below 650 °C at taenite grain boundaries with K–S or N–W orientations with respect to the parent taenite grains (McCoy et al. 2011). Equilibration of kamacite, taenite, and phosphide continued until 510 °C. Below that temperature, Ni gradients in taenite grew and kamacite precipitated in taenite grains below 500 °C with K–S or N–W orientations in the taenite. Phosphide compositions above 40 wt% Ni indicate continuing growth below approximately 400 °C.

Babb's Mill (Blake's Iron) (Ungrouped)

Babb's Mill (Blake's Iron), which contains 10.7 wt% Ni and 0.02 wt% P, has a totally recrystallized structure of taenite grains on grain boundaries in polycrystalline kamacite with a grain size of 10–20 μm. As it is not related to any other iron, we have no direct information about its original structure. The absence of any trace of the original Widmanstὶtten pattern shows that it was heated above 700 °C, so that kamacite completely dissolved. On cooling, according to the Fe-Ni phase diagram (Fig. 12) (Romig and Goldstein 1980), kamacite would have formed at taenite grain boundaries at about 520 °C. Electron-probe analyses of kamacite and taenite show that kamacite grew at the expense of taenite, as the meteorite cooled between 500 and 400 °C.

Ternera (IVB) and Babb's Mill (Troost's Iron) (Ungrouped)

These iron meteorites have very similar Ni and P contents (17.2 versus 17.1 wt% Ni, 0.2 versus 0.13 wt% P; Table 2) and very similar finely polycrystalline microstructures with grain sizes of 5–10 μm. As Ternera is a high-Ni member of chemical group IVB, we can assume that it originally resembled the IVB ataxite Weaver Mountain, which has similar Ni and P contents (17.5% Ni, 0.14% P; Yang et al. 2010) and contains kamacite plates 5–10 μm in width and taenite of micrometer size in the plessite with the same orientation as the original parent taenite crystal (Buchwald 1975; Goldstein and Michael 2006).

Although Babb's Mill (Troost's Iron) is an ungrouped iron, it is closely related to South Byron and ILD 83500, which have similar trace element concentrations (Wasson et al. 1989). South Byron

contains oriented kamacite platelets in a fine plessite matrix (Buchwald 1975), as does ILD 83500 (Clarke 1984). The microstructural and chemical similarities between Babb's Mill (Troost's Iron) and Ternera imply that Babb's Mill (Troost's Iron) once had an ataxite structure like Weaver Mountains, and that it was also reheated and recrystallized.

As both irons contain equiaxed crystals of kamacite, taenite, and phosphide with no indication of a previous ataxite microstructure, we infer that they were heated above 575 °C, so that taenite was spheroidized and changed Ni content to form homogeneous grains about 10 μm in size with diverse orientations. Given that phosphides have nucleated and grown on grain boundaries, we can infer that Ternera was heated above 700 °C and Babb's Mill (Troost's Iron) above 625 °C, so that the original phosphides dissolved. During cooling, kamacite nucleated on taenite grain boundaries with K–S or N–W orientations relative to the parent taenite. Ni gradients formed in taenite, and kamacite nucleated with K–S or N–W orientations in the taenite grains. Equilibration of kamacite, taenite, and phosphide continued until approximately 510 °C (Table 4). Phosphide compositions and nanometer-scale enrichments of Ni in taenite grain boundaries up to 40% Ni indicate continued growth below approximately 400 °C.

Temperature–Time History

All six iron meteorites have microstructures that are consistent with reheating of slowly cooled irons followed by simple monotonic cooling after the peak temperatures were reached. We cannot exclude more complicated thermal histories or multiple reheating events, but see no reason to invoke them. No Widmanstätten kamacite formed on cooling, as the parent taenite grains were too small ($\cup$20 μm in width) and many favorable nucleation sites existed at the grain boundaries. Estimates of the peak reheating temperatures from the discussions above are summarized in Table 6.

The equilibration temperatures calculated from the average Ni concentration in the taenite particles and the minimum Ni concentration in the taenite particles are lower than the peak temperatures, except for Maria Elena, which was the least reheated iron (Table 6). For Maria Elena, the bulk Ni in taenite provides us with our best estimate of the lower limit for the peak reheating temperature. Babb's Mill (Blake's Iron), Babb's Mill (Troost's Iron), Fuzzy Creek, and Ternera have equilibration temperatures inferred from average and minimum Ni concentrations that are all 520 20 °C. As the four irons were reheated to above 625–700 °C, it seems unlikely that the four irons were held at 520 20 °C for any extended period. The average and minimum Ni concentrations of taenite depend on the grain size of the taenite and the cooling rate of the meteorite. As the taenite grain size of Babb's Mill (Blake's Iron), Babb's Mill (Troost's Iron), Fuzzy Creek, and Ternera are similar (mostly 5–10 μm; Table 6), the cooling rates of the four meteorites are most probably quite similar. The cooling rates were, however, rapid enough that the centers of the taenite grains did not increase in Ni content as would be required by equilibration at lower temperatures. On the other hand for Maria Elena and Hammond, the equilibration temperatures determined from the minimum Ni content in taenite are lower by 50–120 °C than those determined by the average taenite compositions. The smaller taenite grain size (2–6 μm; Table 6) of these two meteorites allows for more rapid equilibration at lower temperatures for the same cooling rate.

For Maria Elena, we can estimate the time and temperature for the growth of taenite particles in kamacite regions by assuming that the size of the taenite particles, nominally 2–5 μm, is directly proportional to $(Dt)^{1/2}$, where D is the diffusion coefficient of Ni in kamacite at a given temperature (Dean and Goldstein 1986) and t is the time. Using diffusion coefficients appropriate for Maria Elena, which contains 0.02 wt% P, reheating times vary from approximately 10,000 yr at 500 °C to approximately 3000 yr at 550 °C. (For P-saturated irons, the times would be approximately 1000 yr at 500 °C and approximately 100 yr at 550 °C.) Even if reheating took place at the maximum temperature, where kamacite is still an equilibrium phase, approximately 700 °C, the reheating time at temperature would be significant, approximately 3 yr for P-saturated irons, and approximately 100 yr for meteorites with <0.02 wt% P.

For the four irons that were reheated above the temperatures at which kamacite is stable, we can estimate the time and temperature necessary to form homogeneous taenite grains of approximately 10 μm size. As a first approximation, we can assume that the growth of taenite is $\simeq (Dt)^{1/2}$, where D is the diffusion coefficient of Ni, which is a function of the P concentration (Dean and Goldstein 1986), and t is the time for diffusion. At 750 °C, it would take about 15 yr for meteorites with P contents of >0.1 wt% and about 135 yr for meteorites with P contents $\cup$0.02 wt% P to remove the Widmanstätten pattern and form 10 μm grains of homogeneous taenite. However, if reheating temperatures reached 1000–1300 °C, growth times are much shorter, 15 days to approximately 1 h, respectively. For Fuzzy Creek, Ternera, and Babb's Mill (Troost's Iron), the time to homogenize an approximately 10 μm taenite grain ranges from as much as 15 yr at 750 °C, 16 days at 1000 °C, and 1.2 h at 1300 °C. For Babb's Mill (Blake's Iron), which has

0.02 wt% P, it would take 135 yr at 750 °C to homogenize a 10 μm taenite grain.

Although techniques are available to calculate cooling rates from the "M" shaped Ni profiles (Figs. 7b and 11c) that developed in taenite during growth of oriented microprecipitates of kamacite (Yang and Goldstein 2006), it is generally not possible to make precise calculations for the reheated irons with the available STEM X-ray data. In almost all cases, the orientation of the kamacite–taenite interfaces with respect to the focused electron probe is unknown, so that accurate distances along the Ni gradient are not available and the local P content in kamacite or taenite is below the detectability limit of the EDS in the electron microscope, so that the kamacite nucleation temperature cannot be calculated. Given these orientation and detectability issues, cooling rates of reheated irons that are determined from Ni profiles have large uncertainties.

The cooling rate for Fuzzy Creek was obtained by modeling the nucleation and growth process of a micrometer-sized kamacite plate that formed inside a taenite grain on cooling after reheating (McCoy et al. 2011). The initial composition of the taenite particle was assumed to be the average taenite composition, 24.5 wt % Ni, for the specific taenite region. P is assumed to be saturated in taenite, as the bulk P content of Fuzzy Creek is 0.18 wt% and phosphide is prevalent in the meteorite. Therefore, kamacite nucleates by mechanism II ($\gamma \rightarrow \gamma + Ph \rightarrow \alpha + \gamma + Ph$) according to Yang and Goldstein (2005), and the nucleation temperature for the kamacite precipitates is about 520 °C (793 K) (Yang and Goldstein 2005). The Fe-Ni and Fe-Ni-P phase diagrams, and the interdiffusion coefficients that control the growth of the WidmanstÌtten pattern are given by Yang et al. (2008). Using the taenite profile matching method (Goldstein and Ogilivie 1965), the measured results match the calculated Ni gradient for a cooling rate of 0.5 K yr^{-1} (500,000 K Myr^{-1}). We estimate the error in this measurement as a factor of 10, i.e., the rate was between 0.05 and 5 K yr^{-1} ($5 \cap 10^4$–$5 \cap 10^6$ K Myr^{-1}), in particular, because the orientation of the kamacite–taenite interface is unknown. On the basis of this one cooling rate measurement, we estimate that Fuzzy Creek cooled over a period of 10^2–10^4 yr. From the general similarity of the Ni profiles in taenite in the reheated irons, where STEM X-ray data were obtained (e.g., Figs. 7b and 11c), we infer that the other reheated irons that we have studied also cooled, after reheating, over periods of approximately 100–10,000 yr.

Cooling over centuries or millennia is consistent with what we inferred about the formation of high-Ni martensite, viz., that reheating was intense enough to allow high-Ni taenite to form on cooling, but not so slow that there was time for the martensite to decompose into a two-phase plessitic structure. We conclude that high-Ni martensite is a characteristic of many impact-heated iron meteorites. (We exclude low-Ni martensite that forms from kamacite in the atmospherically heated rims of iron meteorites.) Martensite has also been observed in low-Ni (< 15 wt%) metal in CH chondrites that was reheated from 500 to 700 °C and then cooled relatively fast in hours to days (Goldstein et al. 2007).

Mechanism of Reheating: Connecting Thermal and Shock Histories

The microstructural features that we described above constrain the thermal histories of the six iron meteorites, but they are not direct indications of shock pressure. Herein, we address the relationship between shock, impact, reheating, and other possible sources of heat. For example, were the six meteorites reheated by shock, some other impact process such as shear deformation or impact heat transferred by conduction, or by a totally different process such as solar heating near perihelion (Buchwald 1971)? Were the six irons reheated by the same process that affected other meteorites? Could an ungrouped reheated iron be a reprocessed impact melt from a chondritic body (Wasson 2000)?

As two of the six reheated irons we studied are IVA irons, and much is known about the primary cooling and reheating of these irons, we focus initially on this chemical group to help understand the thermal history of the irons we studied. Unfortunately, there is no classification scheme for comparing the shock metamorphic histories of iron meteorites as there is for silicate-rich meteorites (StÎffler et al. 1991). We have therefore compiled constraints on the shock or reheating history of IVA irons. The following indicators were used: cloudy taenite (Goldstein et al. 2009), M-shaped Ni profiles in taenite (Yang et al. 2008), Neumann twin lamellae in kamacite, martensite, shock-hatched kamacite which results from the transformation above 13 GPa to the ε high-pressure Fe-Ni phase, recrystallization in kamacite and taenite, microprecipitates of taenite in kamacite (as described above), shock melting of troilite, and deformation of the WidmanstÌtten pattern (Buchwald 1975).

After eliminating IVA irons that Buchwald (1975) identified as terrestrially reheated as they show reactions between weathering oxides and heated metal, we assembled the irons according to their shock and reheating features. Four groups appear to represent most of the variation among the IVA irons (Table 7). Stage 1 irons have all the features associated with normal slowly cooled and unshocked irons: kamacite with Neumann twin lamellae, taenite with M-shaped Ni profiles and cloudy taenite borders, and troilite nodules that are

Table 7. Progressive stages of shock and reheating in IVA irons[a].

Stage	Taenite	Cloudy taenite	Kamacite
1	Lamellae have M-shaped Ć Ni profiles	Present	Monocrystalline with Ć Neumann twin lamellae
2	Lamellae have M-shaped Ć Ni profiles	Absent	Shock-hatched $\alpha \rightarrow \varepsilon \rightarrow \alpha$
3	Recrystallized lamellae Ć WidmanstÌtten Ć preserved	Absent	Largely crystallized with Ć taenite microprecipitates Ć on grain boun
4	No trace of Ć WidmanstÌtten pattern	Absent	Totally recrystallized

[a]Type 1: Bishop Canyon, Boogaldi, Bristol, Bushman Land, Charlotte, Chinautla, Duchesne, Duel Hill (1854), Hill City, Iron River, La Grange, Mantos Blanc Gibeon, Jamestown, Muonionalusta, Obernkirchen, Otchinjau, Putnam County, Seneca Township. Type 2–3: Serrania de Varas, Bodaibo. Type 3: CratheÇs (19
[b]Postshock residual temperature of whole meteorite.
[c]Inferred from Ternera.

mostly monocrystalline. Stage 2 irons mostly have shock-hatched kamacite indicating they were shocked above 13 GPa, troilite nodules that are largely shock melted, and normal M-shaped Ni profiles in taenite when analyzed using EPMA, but their cloudy taenite is either modified or absent. One stage 2 iron, Muonionalusta, also contains stishovite, which forms above 10 GPa (Holtstam et al. 2003).

Stage 3 irons are characterized by recrystallized taenite lamellae, partly or wholly recrystallized kamacite plates with microprecipitates of taenite on grain boundaries, and troilite nodules that are completely shock melted. This stage is well represented by Maria Elena as its troilite nodules were shock melted and injected mm to cm into the surrounding kamacite (Buchwald 1975). Buchwald also notes that the kamacite around the troilite nodules is particularly well recrystallized showing that reheating can plausibly be attributed to shock deformation.

Stage 4 irons are characterized by complete recrystallization of kamacite and taenite and a complete lack of a WidmanstÌtten pattern. Fuzzy Creek is the only example in group IVA. We lack data on troilites in Fuzzy Creek, but as Ternera has shock-melted troilite (Buchwald 1975) and a similar recrystallized microstructure, we suggest that the troilite in stage 4 irons would have been completely shock melted and mobilized.

Inspection of Buchwald's table of data for IVA irons (1975, volume 1, appendix 1) shows that some irons do not completely fit the criteria for one of these four stages. For example, Gibeon is listed as lacking shock-hatched kamacite even though we classify it as stage 2. However, in his Supplement in volume 3, Buchwald describes a Gibeon sample with shock-hatched kamacite. We list Altonah as stage 2, although Buchwald did not note any shock-hatched kamacite. Shock-hatched kamacite may be heterogeneously distributed as reported by Jain and Lipschutz (1970). Hill City appears to be a normal stage 1 iron although its troilite was shock melted (Buchwald 1975). New Westville appears to have shock-hatched kamacite, even though it has normal cloudy taenite. These exceptions may result from heterogeneous shock levels or local thermal variations due to proximity to shock-melted troilite.

Some irons show clear evidence for localized impact heating via deformation rather than shock. For example, in Kaalijarv, recrystallization is concentrated in shear zones that formed during terrestrial impact (Buchwald 1975). However, examples of IVA irons with plastically deformed WidmanstÌtten patterns are sprinkled throughout the stages in Table 7 suggesting that this was not a major source of reheating. It also seems unlikely that cooling from approximately 600 to 700 °C over 10^{2-4} yr, as experienced by the stage 3 and 4 irons that we studied, could result from solar heating. We cannot exclude the possibility that some stage 3 irons were recrystallized because of thermal conduction from strongly heated stage 4 or impact melted material. However, the most plausible explanation for extensively recrystallized irons like Maria Elena is that they were very strongly shocked, as suggested by Jain and Lipschutz (1970).

Heymann et al. (1966) inferred that recrystallized irons were heated above 500 °C by shock pressures that exceeded 75 GPa. If the initial temperature was 200 K, rather than the value of 363 K they assumed, this shock pressure would have been 95 GPa, given that an increase

in residual temperature of 200 K requires an increase in shock pressure of approximately 25 GPa (McQueen et al. 1962). For a peak temperature of 700 °C, as we inferred for Babb's Mill (Blake's Iron), for example, the required shock pressure would be approximately 120 GPa. The other five reheated irons (Table 6) were shocked to at least 105 GPa. These shock pressures are based on the assumption that the metal was entirely solid. If the target body was a porous pile of metal fragments that was welded together by shock, the required shock pressures would be lower. For comparison, estimates for the pressure required to totally melt chondrites range from 75 to 90 GPa (Stîffler et al. 1991), or perhaps half this value (Sharp and DeCarli 2006), to as high as 130–140 GPa (Bezaeva et al. 2010).

We cannot exclude the possibility that the stage 3 iron, Social Circle (IVA), was recrystallized at perihelion by solar heating (Buchwald 1975). However, as its troilite nodules were totally shock-melted, we rely on Occam's Razor to argue for recrystallization during shock heating. In the case of Ternera, as noted above, and Hammond there is evidence for shock melting of troilite (Buchwald 1975). In contrast, for Fuzzy Creek, Babb's Mill (Troost's Iron), and Babb's Mill (Blake's Iron), troilite has not been described, and so we cannot exclude a heat source besides shock. However, it seems probable that they are stage 4 irons, which were intensely shocked.

There are no irons in group IVA or any other group (excluding IAB and IIE) with dendritic textures indicating that they were totally or largely melted by impact. We can also exclude the possibility that the ungrouped irons, Babb's Mill (Blake's Iron), and Babb's Mill (Troost's Iron) might be reprocessed impact melts (Wasson 2000). As their grain size of 10–20 μm is so much smaller than the dendrites that would form in a meter-sized molten metallic body (~0.1–1 mm), these irons could not have formed by grain coarsening on cooling after solidification. They must have been reheated and recrystallized.

Nature of Impacts on Parent Bodies

Group IIIAB and IVA irons have a significant number of shocked meteorites (~50% of IVAs are stage 2–4) and are the only two groups that show prominent clusters in the cosmic-ray exposure ages. Keil et al. (1994) therefore suggested that the IIIAB and IVA cores (or large fragments of them) were shocked during the impact that exposed the irons to cosmic rays as meter-sized meteoroids 650 and 400 Ma. However, meter-sized hot irons should cool at approximately 0.1 °C s^{-1} (see, e. g., Scott 1982), and not at ≈0.5 °C yr^{-1}, like Fuzzy Creek. To cool by conduction at ≈0.5 °C yr^{-1}, the recrystallized irons must have been part of km-sized reheated metallic masses. If the reheated irons that we studied are representative, it is likely that the majority of shocked irons in groups IIIAB and IVA were shocked before the impact that exposed them to cosmic rays. There are several other arguments against the suggestion of Keil et al. (1994), which are discussed below.

If IVA irons had been meter-sized objects after they were shocked and heated, their shock and reheating effects should resemble those in Canyon Diablo samples that were shocked on impact with the Earth. However, comparison of Table 7 with descriptions of shocked Canyon Diablo samples (Buchwald 1975, pp. 390–397) shows several differences that point to slower postshock cooling rates for the IVA irons. First, there are no irons in group IVA or any other group with kamacite that was transformed to low-Ni martensite by preterrestrial shock heating ($\alpha \rightarrow \gamma \rightarrow \alpha_2$), although some meteorites from crater forming impacts on Earth do have this form of martensite. We infer that if any irons were shock heated in space, so that low-Ni martensite formed from kamacite, they cooled slowly so that the low-Ni martensite reverted back to kamacite. Second, there are no Canyon Diablo samples that developed microprecipitates of taenite on recrystallized kamacite grain boundaries, presumably because the Canyon Diablo samples cooled faster. Third, some Canyon Diablo samples show steep gradients in their alteration effects (Heymann et al. 1966; Buchwald 1975), which are not observed in other irons.

Most shock heating occurs when the largest bodies are catastrophically broken up as the specific energy necessary for breakup of asteroidal bodies larger than a kilometer in size increases with increasing size (e.g., Bottke et al. 2005). Thus, it is likely that the IVA and IIIAB irons were shocked when the metallic bodies in which they cooled were destroyed. If these events occurred, at 400–650 Ma we should expect to see families of metallic M-type asteroids, for example, the family produced by the 480 Myr breakup of the L chondrite body (Nesvorný et al. 2009). The absence of metallic families of asteroids suggests that the IVA and IIIAB metallic bodies that were broken up at 400 and 650 Ma were relatively small, perhaps a few kilometers in size. As we have samples from near the surface and from the deep interior of metallic bodies that were approximately 50–300 km in diameter when the irons cooled (Yang et al. 2008), the bodies that broke up at 400 and 650 Ma were probably composed of metallic fragments prior to break-up.

Obviously more studies of strongly shocked IIIAB and IVA irons are needed to test whether they cooled over years or hours after reheating. Without such studies, we cannot exclude the possibility that metallic bodies, approximately 50–300 km, were broken up in the

asteroid belt at 400 and 650 Ma. However, given the arguments above and the evidence discussed below that the parent bodies that differentiated to form metallic cores were broken up while hot, we favor major impacts on the 50–300 km metallic bodies before the impacts that exposed the irons to cosmic rays.

Histories of Group IVA and IVB Irons

Yang et al. (2008) inferred from WidmanstÌtten-derived cooling rates and thermal and fractional crystallization models that the IVA irons were the product of three impacts. The first was a hit-and-run glancing impact between protoplanets that generated a molten metallic body approximately 300 km across that lacked a silicate mantle at 4.5 Gyr, possibly a few million years after melting began. The second impact occurred after this body had cooled below 200 °C, perhaps only 20 Myr later. It created a fragment >30 km across or more plausibly a rubblepile asteroid with fragments from diverse depths. The third impact 400 Ma generated a swarm of meter-sized metallic fragments some of which drift into a major resonance at the inner edge of the asteroid belt and deliver meteorites to the Earth (Yang et al. 2008). The thermal histories of Maria Elena and Fuzzy Creek and other arguments discussed above clearly point to the second impact as the one that shocked and reheated the IVA irons.

The primary cooling rates of the IVA irons and the proposed early history of Yang et al. (2008) are remarkably consistent with the Pb-Pb ages of troilite inclusions in two IVA irons (Blichert-Toft et al. 2010). Blichert-Toft et al. (2010) obtained a Pb-Pb age of 4565.3 0.1 Myr for Muonionalusta, and inferred that it had cooled to the Pb closure temperature of approximately 300 °C within 2–3 Myr after calcium-aluminum-rich inclusion (CAI) formation. Given the Hf-W isotopic data that constrain core formation to <1 Myr after CAI formation (Burkhardt et al. 2008), we can infer that the first impact that created the 300 km molten body must have occurred 1–2 Myr after CAIs, and that Muonionalusta cooled below 300 °C at >500 °C Myr^{-1}. Yang et al. (2008) did not measure the cooling rate of Muonionalusta, but its Ni concentration of 8.4% and the Ni-cooling rate relationship of Yang et al. imply that it cooled at approximately 500 °C Myr^{-1}. Bodies that were large enough to have been melted by ^{26}Al would have had radii of >15 km (Sanders and Taylor 2005), and their cores would have cooled at <150 °C Myr^{-1} assuming they had silicate mantles (Haack et al. 1990). Thus, the Pb-Pb age of Muonionalusta requires that the IVA irons cooled without a silicate mantle.

Blichert-Toft et al. (2010) determined a Pb-Pb age of 4544 7 Myr for a troilite inclusion from the Gibeon IVA iron. They inferred that this age resulted from shock melting of troilite in Gibeon, approximately 20 Myr after CAIs formed. As Gibeon was probably located approximately 10 km below the surface of the IVA body when it cooled (Yang et al. 2008), this impact may have demolished the body. We note that Muonionalusta also contains stishovite (Holtstam et al. 2003) and shock-melted troilite nodules (Buchwald 1975), but they lack the vugs caused by impact vaporization found in some Gibeon sulfides (Petaev and Marvin 1997).

If the 150 km radius IVA body was destroyed long before the iron meteorites were exposed to cosmic rays, as argued above, the IVA body may have been destroyed very early in the asteroid belt when the total mass of asteroids was very much higher (Yang et al. 2008). However, another possibility is that the iron meteorite parent bodies were formed at 1.5–2 AU (Bottke et al. 2006) and then destroyed in this region after they cooled. Given that 50% of the IVA irons were shocked above 13 GPa (Table 7) and Fuzzy Creek was reheated above 650 °C even though it was located tens of km below the surface, the destruction of the IVA metallic core probably involved a conventional head-on collision rather than a hit-and-run glancing collision with a larger body (see Asphaug et al. 2006). Impacts in the region of the terrestrial planets would inevitably have involved higher impact velocities than those in the asteroid belt causing higher shock pressures and more extensive heating.

The IVB irons had a similar history to the IVA irons in that their original parent body accreted <1 Myr after CAI formation (Markowski et al. 2006) and the irons cooled in a metallic body that lacked a silicate mantle. However, the IVB core probably solidified prior to the impact that separated core and mantle, and the metallic body in which the irons cooled was smaller, only 65 15 km in radius (Yang et al. 2010). As the core appears to have solidified outwards, Ternera, the only IVB sample reheated above 575 °C, would have been located relatively close to the surface. Seven of eight other IVB irons retained their cloudy taenite (Yang et al. 2010). If these samples are representative, the more limited impact damage among IVB irons would be consistent with the smaller specific impact energy needed to destroy a smaller parent body or excavate deeply buried material. We lack radiometric ages to constrain the time of the major impacts, but infer that they were early, as for group IVA irons. The IVB irons have diverse cosmic-ray exposure ages that are uncorrelated with bulk Ni, suggesting that a small remnant suffered many smaller impacts during the last 1 Gyr (Voshage and Feldmann 1979).

The three ungrouped irons also cooled over centuries to millennia. If they are typical, it is likely that most

impacts that shocked iron meteorites predated the impacts that exposed the irons to cosmic rays. As for groups IVA and IVB, it is plausible that impact reheating occurred during the major impact that shattered the parent metallic bodies. These impacts may have occurred soon after the irons had cooled slowly and developed plessitic intergrowths that would readily recrystallize during reheating.

Acknowledgments—Financial support from NASA through grants NNX08AG53G (J. I. Goldstein, P. I.), NNG06GF56G (T. J. McCoy), and NNX08AI43G (E. R. D. Scott, P. I.) is acknowledged. We thank Laurence Garvie (Arizona State University), Joseph Boesenberg and Denton Ebel (American Museum of Natural History), and Valerie Reynolds (Colby College) for helpful discussions and assistance with the source(s) of the Babb's Mill specimens. We thank Alice Kilgo (Sandia) for metallographic preparation, and Michael Rye and Garry Bryant (both from Sandia) for FIB preparation. Our research was aided considerably by Vagn Buchwald's Handbook of Iron Meteorites, as it contributed enormously to our understanding of cosmically and terrestrially reheated iron meteorites. We thank Henning Haack, Alan Rubin, and an anonymous referee for their helpful and detailed reviews.

Editorial Handling—Dr. Nancy Chabot

REFERENCES

Asphaug E., Agnor C. B., and Williams Q. 2006. Hit-and-run planetary collisions. *Nature* 439:155–160.

Axon H. J. 1962. Dendritic structure in the Nedagolla ataxite. *Nature* 196:567–568.

Bezaeva N. S., Badjukov D. D., Rochette P., Gattacceca J., Trukhin V. I., Kozlov E. A., and Uehara M. 2010. Experimental shock metamorphism of the L4 chondrite Saratov induced by spherical shock waves up to 400 GPa. *Meteoritics & Planetary Science* 45:1007–1020.

Blake W. P. 1886. Description of a meteorite from Green County, Tennessee (Blake's Iron). *American Journal of Science* 31:41–46.

Blichert-Toft J., Moynier F., Lee C.-T. A., Telouk P., and AlbarÉde F. 2010. The early formation of the IVA iron body. *Earth and Planetary Science Letters* 296:469–480.

Bottke W. F., Durda D. D., Nesvorny¨ D., Jedicke R., Morbidelli A., Vokrouhlicky D., and Levison H. F. 2005. Linking the collisional history of the main asteroid belt to its dynamical excitation and depletion. *Icarus* 179:63–94.

Bottke W. F., Nesvorny¨ D., Grimm R. E., Morbidelli A., and O'Brien D. P. 2006. Iron meteorites as remnants of planetesimals formed in the terrestrial planet region. *Nature* 439:821–824.

Buchwald V. F. 1967. *Study of six iron meteorites*. Analecta Geologica, No. 2. Copenhagen: Mineralogisk Museum pp. 21–31.

Buchwald V. F. 1971. Tritium loss resulting from cosmic annealing, compared with the microstructure and microhardness of six iron meteorites. *Chemie der Erde* 30:33–57.

Buchwald V. F. 1975. *Handbook of iron meteorites. Their history, distribution, composition and structure*. Berkeley⊇ Los Angeles, CA: University of California Press.

Burkhardt C., Kleine T., Bourdon B., Palme H., Zipfel J., Friedrich J., and Ebel D. 2008. Hf–W mineral isochron for Ca, Al rich inclusions: Age of the solar system and the timing of core formation in planetesimals. *Geochimica et Cosmochimica Acta* 72:6177–6197.

Clarke R. S. 1984. Petrographic description of ILD 83500. *Antarctic Meteorite Newsletter* 7:29. http://www.lpi.usra.edu/meteor/metbull.php.

Clarke R. S. Jr. and Goldstein J. I. 1978. Schreibersite growth and its influence on the metallography of coarse-structured iron meteorites. *Smithsonian Contributions to the Earth Sciences* 21:1–80.

Cliff G. and Lorimer G. W. 1975. The quantitative analyses of thin specimens. *Journal of Microscopy* 103:203–207.

Cohen E. 1905. *Meteoritenkunde*, Heft III. Stuttgart: Schweizerbartsche Verlagshandlung. pp. 104–107.

Crank J. and Nicolson P. A. 1947. Practical method for numerical evaluation of solutions of partial differential equations of the heat-conduction type. *Proceedings of the Cambridge Philosophical Society* 43:50–67.

Dean D. C. and Goldstein J. I. 1986. Determination of the interdiffusion coefficients in the Fe Ni and Fe Ni P systems below 9000 C. *Metallurgical Transactions* 17A:1131–1138.

Doan A. S. and Goldstein J. I. 1970. The ternary phase diagram, Fe-Ni-P. *Metallurgical Transactions* 1:1759–1767.

Goldstein J. I. and Michael J. R. 2006. The formation of plessite in meteoritic metal. *Meteoritics & Planetary Science* 41:553–570.

Goldstein J. I. and Ogilivie R. E. 1965. Diffusion in the Fe-Ni system at 1 Atm and 40 Kbar pressure. *Transactions of the Metallurgical Society. American Institute of Metallurgical Engineers* 233:812–820.

Goldstein J. I., Jones R. H., Kotula P. G., and Michael J. R. 2007. Microstructure and thermal history of metal particles in CH chondrites. *Meteoritics & Planetary Science* 42:913–933.

Goldstein J. I., Yang J., Kotula P. G., Michael J. R., and Scott E. R. D. 2009. Thermal histories of IVA iron meteorites from transmission electron microscopy of the cloudy zone microstructure. *Meteoritics & Planetary Science* 44:343–358.

Haack H., Rasmussen K. L., and Warren P. H. 1990. Effects of regolith⊇megaregolith insulation on the cooling history of differentiated asteroids. *Journal of Geophysical Research* 95:5111–5124.

Heymann D., Lipschutz M. E., Nielsen B., and Anders E. 1966. Canyon Diablo meteorite: Metallographic and mass spectrometric study of 56 fragments. *Journal of Geophysical Research* 71:619–641.

Heyward T. R. and Goldstein J. I. 1973. Ternary diffusion in the α and γ phases of the Fe-Ni-P system. *Metallurgical Transactions* 4:2335–2343.

Holtstam D., Broman C., SÎderhielm J., and Zetterqvist A. 2003. First discovery of stishovite in an iron meteorite. *Meteoritics & Planetary Science* 38:1579–1583.

Jain A. V. and Lipschutz M. E. 1970. On preferred disorder and the shock history of chemical group IVA meteorites. *Geochimica et Cosmochimica Acta* 34:883–892.

Keil K., Haack H., and Scott E. R. D. 1994. Catastrophic fragmentation of asteroids: Evidence from meteorites. *Planetary and Space Science* 42:1109–1122.

Leroux H. 2001. Microstructural shock signatures of major minerals in meteorites. *European Journal of Mineralogy* 13:253–272.

Lewis C. F. and Moore C. B. 1971. Chemical analyses of thirty-eight iron meteorites. *Meteoritics* 6:195–205.

Malvin D. J., Wang D., and Wasson J. T. 1984. Chemical classification of iron meteorites. XöMultielement studies of 43 irons, resolution of group IIIE from IIIAB, and evaluation of Cu as a taxonomic parameter. *Geochimica et Cosmochimica Acta* 48:785–804.

Markowski A., QuittÅ G., Halliday A. N., and Kleine T. 2006. Tungsten isotopic compositions of iron meteorites: Chronological constraints vs. cosmogenic effects. *Earth and Planetary Science Letters* 242:1–15.

McCoy T. J., Walker R. J., Goldstein J. I., Yang J., McDonough W. F., Rumble III D., Chabot N. L., Ash R. D., Corrigan C. M., Michael J. R., and Kotula P. G. 2011. Group IVA irons: New constraints on the crystallization and cooling history of an asteroidal core with a complex history. *Geochimica et Cosmochimica Acta* (in press).

McQueen R. G., Zukas E., and Marsh S. 1962. *Residual temperature of shock-loaded iron*. Symposium on Dynamic Behavior of Materials. Philadelphia, Pennsylvania: American Society for Testing and Materials. pp. 306–316.

Mitchell B. S. 2003. *An introduction to materials engineering and science: For chemical and materials engineers*, III D. Hoboken, NJ: Wiley-Interscience. 954 p.

Miyake G. T. and Goldstein J. I. 1974. Nedagolla, a remelted iron meteorite. *Geochimica et Cosmochimica Acta* 38:747–755.

Nesvorný D., Vokrouhlický D., Morbidelli A., and Bottke W. F. 2009. Asteroidal source of L chondrite meteorites. *Icarus* 200:698–701.

Oikawa H. 1982. Review on lattice diffusion of substitutional impurities in Fe. A summary report. *Technical Reports of Tohoku University* 47:215–224.

Perry S. H. 1944. *The metallography of meteoric iron*. Washington, D.C.: United States National Museum, Bulletin 184, Smithsonian Institution.

Petaev M. I. and Marvin U. B. 1997. Mineralogy and origin of brassy, sulfide-rich masses in the Gibeon IVA iron (abstract). 28th Lunar and Planetary Science Conference. p. 1093.

Rasmussen K. L., Malvin D. J., Buchwald V. F., and Wasson J. T. 1984. Compositional trends and cooling rates of group IVB iron meteorites. *Geochimica et Cosmochimica Acta* 48:805–813.

Reisener R. J. and Goldstein J. I. 2003. Ordinary chondrite metallography: Part 1. Fe-Ni taenite cooling experiments. *Meteoritics & Planetary Science* 38:1669–1678.

Romig A. D. and Goldstein J. I. 1980. Determination of the Fe-Ni and Fe-Ni-P phase diagrams at low temperatures (700 to 300 °C). *Metallurgical Transactions* 11A:1151–1159.

Sanders I. S. and Taylor G. J. 2005. Implications of ^{26}Al in nebular dust: Formation of chondrules by disruption of molten planetesimals. In *Chondrites and the protoplanetary disk*, edited by Krot A. N., Scott E. R. D., and Reipurth B., ASP Conference Series, vol. 341. San Francisco: Astronomical Society of the Pacific. pp. 915–932.

Schaudy R., Wasson J. T., and Buchwald V. F. 1972. The chemical classification of iron meteorites, VI. A reinvestigation of irons with Ge concentrations lower than 1 ppm. *Icarus* 17:174–192.

Schrader D. L., Lauretta D. S., Connolly H. C. Jr., Goreva Y. S., Hill D. S., Domanik K. J., Berger E. L., Yang H., and Downs R. T. 2010. Sulfide-rich metallic impact melts from chondritic parent bodies. *Meteoritics & Planetary Science* 45:743–758.

Scott E. R. D. 1982. Origin of rapidly solidified metal-troilite grains in chondrites and iron-meteorites. *Geochimica et Cosmochimica Acta* 46:813–823.

Scott E. R. D., Wasson J. T., and Buchwald V. F. 1973. The chemical classification of iron meteoritesöVII. A reinvestigation of irons with Ge between 25 and 80 ppm. *Geochimica et Cosmochimica Acta* 37:1957–1983.

Sharp T. G. and DeCarli P. S. 2006. Shock effects in meteorites. In *Meteorites and the early solar system II*, edited by Lauretta D. S. and McSween H. Y. Jr. Tucson, AZ: The University of Arizona Press. pp. 653–677.

Shepard C. U. 1847. Report on meteorites. *American Journal of Science* (Series 2) 4:74–87.

StÎffler D., Bischoff A., Buchwald V., and Rubin A. E. 1988. Shock effects in meteorites. In *Meteorites and the early solar system*, edited by Kerridge J. F. and Matthews M. S. Tucson, Arizona: The University of Arizona Press. pp. 165–202.

StÎffler D., Keil K., and Scott E. R. D. 1991. Shock metamorphism of ordinary chondrites. *Geochimica et Cosmochimica Acta* 55:3845–3867.

Troost G. 1845. Description etc. of Charlotte, Smithville, Babb's Mill, and Walker County iron meteorites. *American Journal of Science* 49:336–346.

Von Rosenburg D. U. 1969. *Methods for the numerical solution of partial differential equations*. New York: American Elsevier Publishing Company Inc.

Voshage H. and Feldmann H. 1979. Investigation of cosmic-ray-produced nuclides in iron meteorites, 3: Exposure ages, meteoroid sizes and sample depth determined by spectrometric analyses of potassium and rare gases. *Earth and Planetary Science Letters* 45:293–308.

Walker R. J., McDonough W. F., Honesto J., Chabot N. L., McCoy T. J., Ash R. D., and Bellucci J. J. 2008. Modeling fractional crystallization of group IVB iron meteorites. *Geochimica et Cosmochimica Acta* 72:2198–2216.

Wasson J. T. 2000. *Iron Meteorites From Antarctica: More Specimens, Still 40% Ungrouped. Workshop on Desert Meteorites*. LPI Contribution 997. Houston, Texas: Lunar and Planetary Institute. pp. 76–80.

Wasson J. T. and Richardson J. W. 2001. Fractionation trends among IVA iron meteorites: Contrasts with IIIAB trends. *Geochimica et Cosmochimimica Acta* 65:951–970.

Wasson J. T., Ouyang X., Wang J., and Jerde E. 1989. Chemical classification of iron meteorites. XIöMulti-element studies of 38 new irons and the high abundance of ungrouped irons from Antarctica. *Geochimica et Cosmochimica Acta* 53:735–744.

Yang J. and Goldstein J. I. 2005. The formation mechanism of the WidmanstÌtten structure in meteorites. *Meteoritics & Planetary Science* 40:239–253.

Yang J. and Goldstein J. I. 2006. Metallographic cooling rates of the IIIAB iron meteorites. *Geochimica et Cosmochimica Acta* 70:3197–3215.

Yang C. W., Williams D. B., and Goldstein J. I. 1996. A revision of the Fe-Ni phase diagram at low temperature. *Journal of Phase Equilibria* 17:522–531.

Yang J., Goldstein J. I., and Scott E. R. D. 2007. Iron meteorite evidence for early catastrophic disruption of protoplanets. *Nature* 446:888–891.

Yang J., Goldstein J. I., and Scott E. R. D. 2008. Metallographic cooling rates and origin of IVA iron meteorites. *Geochimica et Cosmochimica Acta* 72:3043–3061.

Yang J., Goldstein J. I., Michael J. R., Kotula P. G., and Scott E. R. D. 2010. Thermal history and origin of the IVB iron meteorites and their parent body. *Geochimica et Cosmochimica Acta* 74:4493–4506.

Zhang J., Williams D. B., and Goldstein J. I. 1993. The microstructure and formation of duplex and black plesite in iron meteorites. *Geochimica et Cosmochimica Acta* 57:3725–3735.

APPENDIXÖBABB'S MILL IRONS

INTRODUCTION

In this Appendix, we explain why we believe that the sample of Babb's Mill (Troost's Iron) described by Buchwald (1975) is mislabeled. We also investigate the thermal history of the forged samples of this meteorite using computer simulation techniques.

Troost (1845) described an approximately 6 kg sample that was plowed up near Babb's Mill. However, Shepard (1847) reported that two samples had been found: the 6 kg sample that was heated and divided, and a 2.7 kg sample that he acquired that was still in its original state. A second iron weighing about 135 kg was plowed up not far from where the other two samples were recovered (Blake 1886). Although the two irons have very different Ni concentrationsöBabb's Mill (Blake's Iron) contains 11% Ni, whereas Babb's Mill (Troost's Iron) contains 17% NiöCohen (1905) inferred that they were from the same fall, because he thought that the structures of the two irons were similar, and Ni-rich ataxites are rare.

Buchwald (1967) disagreed with Cohen (1905) and argued that the Babb's Mill (Blake's Iron) and Babb's Mill (Troost's Iron) were entirely separate irons. He confirmed that samples from the 6.2 kg Babb's Mill (Troost's Iron) had been artificially reheated, and inferred that the sample studied by Perry (1944) from the American Museum of Natural History (AMNH 98) was from the 2.7 kg mass described by Shepard, which had not been forged. Subsequently Buchwald (1975) described in detail the microstructure of Babb's Mill (Blake's Iron), the AMNH sample of Babb's Mill (Troost's Iron), and the artificially reheated Babb's Mill (Troost's Iron). Our studies confirm Buchwald's conclusions about the artificially reheated Troost's Iron and also that Babb's Mill (Blake's Iron) is a separate fall. However, we are persuaded that the AMNH sample of Troost's Iron, which he described as the type specimen, is mislabeled.

SAMPLES OF BABB'S MILL

Table A1 shows the seven Babb's Mill samples that we studiedösix labeled Troost's Iron and the Blake's Iron sampleöand summarizes their microstructure. Bulk Ni and P concentrations determined from EPMA are given in Table A2. We find that the six samples of Babb's Mill (Troost's Iron), which all lack a WidmanstÌtten pattern, can be divided into three groups according to the optical images of their microstructure visible after etching (Figure A1): (a) AMNH 98-1, which has a plessite microstructure characteristic of many high-Ni irons; (b) samples with a recrystallized microstructure; and (c) artificially heated samples.

Table A1. Babb's Mill meteorite samples.

Meteorite name	Source	Microstructure
Babb's Mill Ć (Blake Iron)	NHMV	Polycrystalline, Ć 2 phase
Babb's Mill Ć (Troost's Iron)[a]	AMNH 98-1	Plessite
Babb's Mill Ć (Troost's Iron)	ASU 2905 USNM 2646	Polycrystalline, Ć 3 phase
Babb's Mill Ć (Troost's Iron)	USNM 962 USNM 3283 USNM 1578	Polycrystalline, 2 phase, Ć

Note: NHMV = Natural History Museum Vienna; AMNH = American Museum USNM = US National Museum of Natural History; ASU = Arizona St + T = kamacite plus taenite; K + T + Ph = kamacite plus taenite plus phosphide $(Fe\text{-}Ni)_3P$.
[a]This sample is mislabelled (see text).

Table A2. Bulk Ni and P content of Babb's Mill Irons from EPMA measurements.

Meteorite name	Source	Bulk Ni (σ, wt%)	Bulk P (σ, wt%)
Babb's Mill Ć (Blake Iron)	NHMV	10.75 0.59	0.02 0.002
Babb's Mill Ć (Troost's Iron)[a]	AMNH 98-1	13.6 0.29	0.02 0.001
Babb's Mill Ć (Troost's Iron)	ASU 2905	17.1 0.38	0.13 0.025
Babb's Mill Ć (Troost's Iron)	USNM 962	17.2 1.66	0.13 0.005

Note: AMNH = American Museum of Natural History; USNM = National Museum of Natural History; ASU = Arizona State University.
[a]This sample is mislabeled (see text).

AMNH 98-1

Figure A1a shows that this iron has a plessite matrix like many other high-Ni irons with spindle-shaped kamacite platelets (Buchwald 1975; fig. 283). The same microstructure of the American Museum of Natural History sample was also shown in plate 26-3 and 26-4 (Perry 1944). The bulk chemical composition

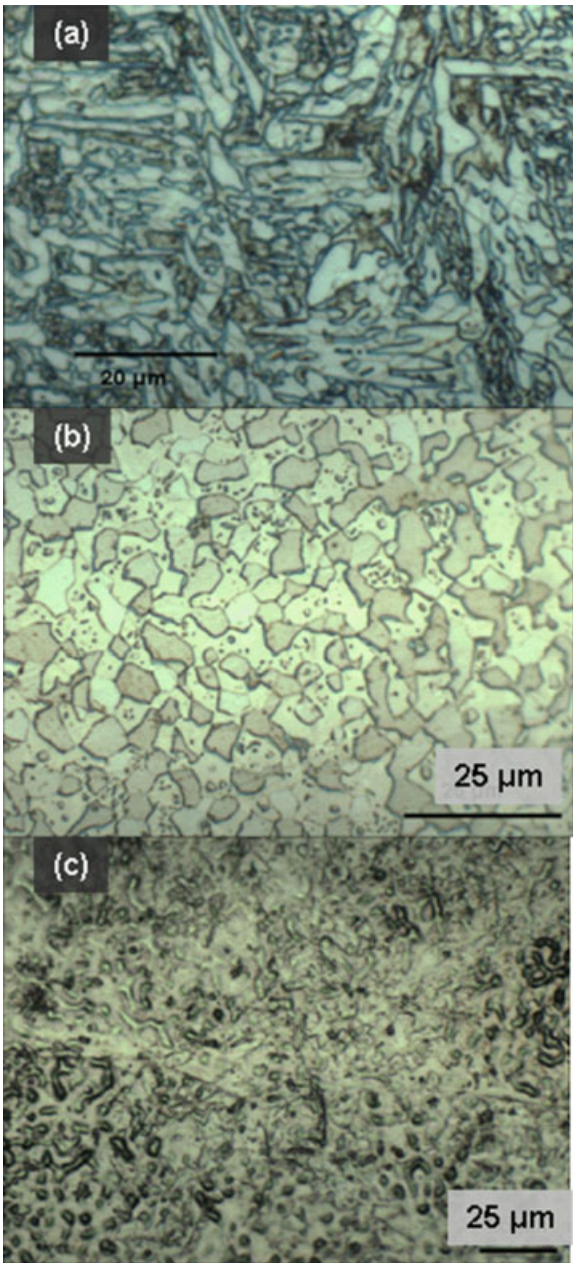

Fig. A1. Reflected-light images of etched sections of three specimens that are all labeled Babb's Mill (Troost's Iron). a) AMNH 98-1 that has an ataxite microstructure, and is not a sample of Babb's Mill (Troost's Iron). b) ASU-2905 that has a two-phase microstructure with small phosphide precipitates, and is a sample of Babb's Mill (Troost's Iron) that was not artificially reheated. c) USNM-962 that is an artificially reheated sample of Babb's Mill (Troost's Iron) shows fuzzy interfaces between kamacite and taenite.

obtained using EPMA is 13.6 0.29 wt% Ni and 0.02 0.001 wt% P, respectively (Table A2). Phosphides are absent, consistent with the low bulk P content measured in this study.

Samples With Recrystallized Microstructure

Two Babb's Mill (Troost's Iron) samples have the recrystallized microstructure shown in Fig. A1b, which we have already described in detail: ASU 2905 and USNM 2646. EPMA data show that ASU 2905 has a bulk concentration of 17.1% Ni and 0.13% P.

Artificially Heated Samples

The artificially heated sample of Babb's Mill (Troost's Iron), USNM 962 (Fig. A1c) shows a polycrystalline two-phase microstructure with diffuse boundaries, which closely resembles that shown by Buchwald (1975). The bulk composition determined using EPMA of this sample is 17.2 wt% Ni and 0.13 wt % P, which is very similar to the bulk compositions of the Babb's Mill (Troost's Iron) sample with a recrystallized microstructure, ASU 2905 (Table A2). Their mean composition, 17.2 1.07 wt% Ni, and 0.13 0.01 wt% P, is very close to the bulk composition given by Buchwald (1975).

We conclude that AMNH 98-1, which has a unique microstructure, is a mislabeled sample for three reasons: (1) The Ni concentration is much lower than those in all the other samples of Babb's Mill (Troost's Iron) samples: 13.6% versus 17.1% Ni. (2) The P concentration is much lower than in all the other samples: 0.02 wt% versus 0.13 wt%. (3) The ASU sample (#2905) was taken from Shepherd's 2.7 kg mass, which was acquired by Amherst College and then by Arizona State University (Garvie, personal communication). The AMNH 98-1 section was taken from a sample that now weighs 52 g and was once part of the Bement Collection (Boesenberg, personal communication). We suggest it may be a mislabeled sample of Deep Springs or another similar ataxite.

THERMAL HISTORY OF ARTIFICIALLY HEATED BABB'S MILL (TROOST'S IRON)

Samples of Babb's Mill (Troost's Iron) with microstructures like that of USNM 962 (Fig. A1c) experienced heat treatment by a blacksmith (Buchwald 1975). Reheating has completely erased the original recrystallized microstructure (Fig. A1b), but a chemical record of the original structure remains. An electron microprobe traverse across a 20 µm region shows anticorrelated variations in the Ni and Co concentrations, which reflect partial homogenization of the chemical variations inherited from the pre-existing high-Co, low-Ni kamacite, and low-Co, high-Ni taenite. P concentrations are uniform. The mean Ni, Co, and P concentrations in USNM 962 are very close to those that

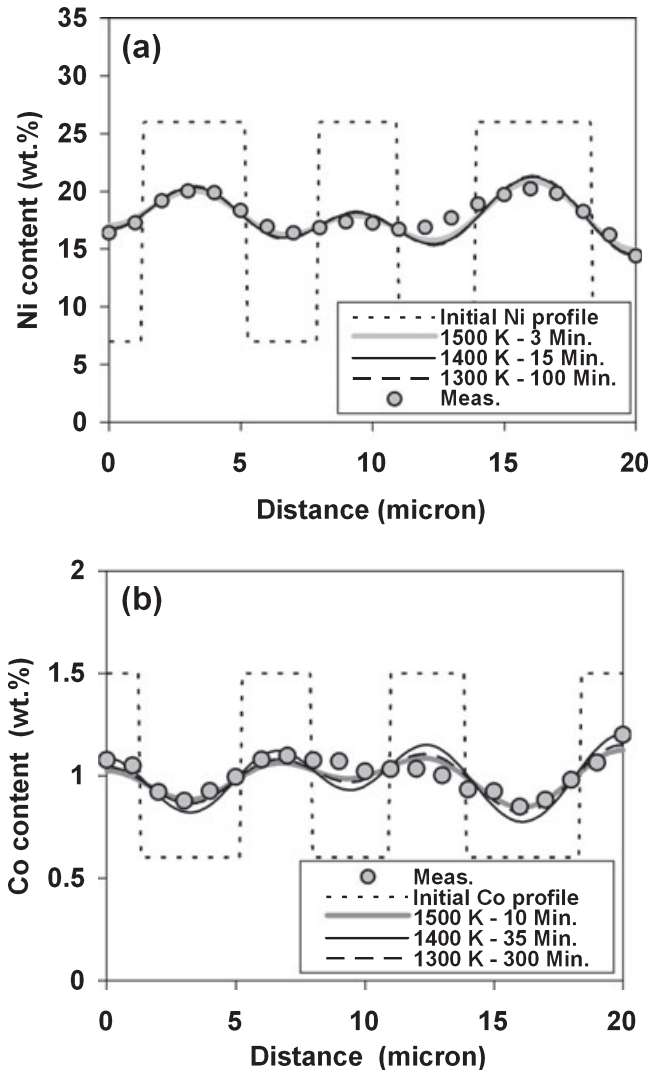

Fig. A2. Comparison between measured Ni and Co concentration profiles (blue dots) for the Babb's Mill (Troost's Iron) sample that was artificially reheated by a blacksmith (USNM 962) and calculated profiles (colored lines) for various heat treatments. The dashed lines show the assumed initial profiles.

were measured in unaltered samples (Table 2). (The Co data were omitted from Table 2 as they were not corrected for the small overlap between FeKβ and CoKα X-ray lines.) We infer that this sample of Babb's Mill (Troost's Iron) was heated above 700 °C so that all the phosphide dissolved and all the kamacite was converted to taenite. Diffusion at these high temperatures homogenized P as it diffuses more rapidly than Ni and Co (Heyward and Goldstein 1973).

We developed a computer code to simulate the homogenization of Ni, Co, and P in a reheated Babb's Mill (Troost's Iron) meteorite (Fig. A1b). To simplify the problem, the low-Ni kamacite and high-Ni taenite are assumed to be initially uniform in composition, as shown by the dashed lines for Ni and Co in Fig. A2. These initial compositions are the average Ni, Co, and P compositions we measured in kamacite and taenite in the kamacite–taenite microstructure shown in Fig. A1b (Table 4). An isothermal heat treatment is assumed to model homogenization by diffusion described by Fick's second law. The Crank and Nicolson (1947) approximation was applied to calculate the partial differential equation and the tri-diagonal matrix algorithm (Von Rosenburg 1969) to solve the finite difference equation. We used the Ni diffusion coefficient from Yang and Goldstein (2005), the Co and P diffusion coefficients from Oikawa (1982), and temperatures ranging from 1300 to 1500 K.

Figure A2 shows the calculated Ni and Co profiles that best match the measured composition profiles of the artificially reheated Babb's Mill (Troost's Iron). We show that 3 min at 1500 K, 15 min at 1400 K, or 100 min at 1300 K give calculated Ni profiles that match the measured Ni profiles. For Co, we estimate that 10 min at 1500 K, 35 min at 1400 K, or 300 min at 1300 K would match the measured Co profiles of the artificially heated Babb's Mill (Troost's Iron) sample. These reheating times are within a factor of 3 from those calculated for Ni diffusion. For P, which diffuses more rapidly, we calculate that 5 min at 1500 K (1227 °C) would produce a uniform concentration. A typical blacksmith's forging heat is in the yellow-orange color range (~1300–1500 K), so that our calculated forging temperatures and times are consistent with the time–temperature cycle used by blacksmiths in the early 1800s.